Published in final edited form as:

NMR Biomed. 2023 June ; 36(6): e4784. doi:10.1002/nbm.4784.

Imaging of sugar-based contrast agents using their hydroxyl proton exchange properties

Linda Knutsson[#,1,2,3], **Xiang Xu**[#,2,4], **Peter CM van Zijl**[2,3], **Kannie WY Chan**[2,5,6,7,8]

[1]Department of Medical Radiation Physics, Lund University, Lund, Sweden

[2]Russell H. Morgan Department of Radiology and Radiological Science, Johns Hopkins University School of Medicine

[3]F.M. Kirby Research Center for Functional Brain Imaging, Kennedy Krieger Institute, Baltimore, US

[4]BioMedical Engineering and Imaging Institute, Icahn School of Medicine at Mount Sinai, New York, NY, United States

[5]Department of Biomedical Engineering, City University of Hong Kong, Hong Kong, China

[6]Hong Kong Centre for Cerebro-Cardiovascular Health Engineering, Hong Kong, China

[7]Tung Biomedical Sciences Centre, City University of Hong Kong

[8]City University of Hong Kong Shenzhen Institute, Shenzhen, China

Abstract

The ability of CEST MRI to detect the presence of millimolar concentrations of non-metallic contrast agents has made it possible to study, noninvasively, important biological molecules such as proteins and sugars, as well as drugs already approved for clinical use. Here, we review efforts to use sugar and sugar polymers as exogenous contrast agents, which is possible based on the exchange of their hydroxyl protons with water protons. While this capability has raised early enthusiasm, for instance about the possibility to image D-glucose metabolism with MRI in a way analogous to PET, experience over the past decade has shown that this is not trivial. On the other hand, many studies have confirmed the possibility to image a large variety of sugar analogues, each with potentially interesting applications to assess tissue physiology. Some promising applications are the study of (i) sugar delivery and transport to assess blood brain barrier integrity, (ii) sugar uptake by cells for their characterization (e.g. cancer vs healthy), as well as (iii) clearance of sugars to assess tissue drainage for instance through the glymphatic system. To judge these opportunities and their challenges, especially in the clinic, it is needed to understand the technical aspects of detecting the presence of rapidly exchanging protons through the water signal in MRI, especially as a function of magnetic field strength. We expect that novel approaches in terms of MRI detection (both saturation transfer and relaxation based), MRI data analysis, and sugar design will push this young field forward in the next decade.

Correspondence to: Kannie WY Chan, Ph.D., Department of Biomedical Engineering, City University of Hong Kong, Hong Kong, China, Phone: +852 34429141, KannieW.Y.C@cityu.edu.hk.

[#]Authors contributed equally

Keywords

Alzheimer's disease; cancer; CEST; D-glucose; glucoCEST; sugars

1. INTRODUCTION

Gadolinium-based contrast agents (GBCAs) have been used clinically for MRI since the late 1980s. As these agents provide specificity and sensitivity by visualizing anatomical and physiological information not available from standard imaging, they have been proven to be extremely valuable for diagnostics. The most common uses for GBCAs in neuroimaging are associated with visualizing disruption of the blood-brain barrier in tumors and enhancement of vessels in MR angiography. However, they can also be employed to assess physiological parameters, such as blood flow, blood volume, and permeability. Today, GBCAs are administered in about 25% of all MRI examinations[1] with approximately 30 million yearly injections worldwide.[2] While these GBCAs are generally considered safe, they have been linked with cases of nephrogenic systemic fibrosis,[3,4] especially in patients with renal diseases. It has also been reported that Gadolinium[5] accumulates in the brain[6–9] and the bones[10] after repeated use. Although no association has been established between clinical findings and these deposits, the regulatory agencies are now issuing warnings for their use. As a consequence, the development of new contrast agents and methods not dependent on Gd use is warranted. A breakthrough towards that goal was achieved by Balaban and co-workers,[11,12] who suggested to use compounds with exchangeable protons (e.g. hydroxyl -OH, amide -NH, amine -NH_2) as MRI contrast agents. They showed that sensitivity-enhanced MRI experiments can be designed to image these millimolar concentration compounds by labeling the exchangeable protons using radiofrequency (RF) and measuring the repeated label transfer to water[12]. Exchange also affects the transverse relaxation time of water[13,14]. In recent years, the interests and efforts for developing exchange-sensitive MRI techniques and exchange agents have increased strongly, leading to a new field of study. Methods include chemical exchange saturation transfer (CEST) MRI,[12,15] chemical exchange sensitive spin-lock (CESL) MRI[16], and even simple T_2-relaxation sensitive MRI[13,17–19] of exogenous exchange agents. Unfortunately, the development and regulatory approval of agents typically takes many years, starting with toxicity assessment and extensive trials. As such, the initial development of CEST agents for human use has focused on agents already approved for other imaging methods or drugs already used in the clinic. Examples are the computed tomography (CT) agents iopamidol[20–23] and iopromide,[24,25] salicylic acids,[26,27] several cancer drugs,[28] and different sugars[29,30] and sugar polymers.

In this review we focus on sugars that have been suggested as exogenous CEST contrast agents in the current MRI literature. Thus, we include for instance the polymer family of dextrans,[31–35] but not glycogen.[36,37] It is important to realize the difference between sugars and conventional contrast agents, namely that some of them are physiologically relevant. For instance, abnormal D-Glc transport and/or utilization in the brain could indicate early neuropathology; cancer cells exhibit aerobic glycolysis, where D-Glc is converted to lactate; hypoglycemia and deficiency of a major glucose transporter (GLUT1) of the blood-brain

barrier (BBB) may lead to epilepsy.[38] Also, a reduction in cerebral glucose metabolism has been reported as one of the earliest signs of Alzheimer's disease.[39] We therefore start the review with an overview of the physiological properties of the different sugars (Section 2). Exchange-based MRI detection in principle offers an opportunity to report on the delivery, transport and metabolism of D-Glc and other types of sugars without the use of either radioactive or metallic labelling. However, while this potential has stirred a lot of excitement, it has to be realized that separation of these three stages of uptake is not trivial and care should be taken not to assume that D-Glc based CEST MRI provides information similar to fluorodeoxyglucose (FDG) based positron emission tomography (PET).

In addition to physiological properties, the magnitude of the MRI effects depends on the MR spectral properties of the exchangeable protons in the agents (Section 3). Knowledge of these is crucial for optimizing the experimental parameters. MR methodological aspects such as pulse sequences, field dependence, and quantification are addressed in Section 4. Importantly, MRI and CEST tend to use acronyms for methods. With respect to such nomenclature, if not already specified in the original paper, we will follow the usual CEST MRI convention of listing either the proton group (amide, amine, etc) or the compound itself before the detection method. For instance, exchange-based saturation studies of D-glucose (D-Glc) would be glucoCEST or glucoCESL, while this would be dexCEST or dexCESL for dextran, etc. For dynamic studies, the nomenclature will be agent based and the detection method deleted, e.g. dynamic glucose enhanced (DGE) will apply to CEST, CESL and contrast-enhanced (CE) relaxation measurements. Section 5 summarizes some promising examples of current preclinical and clinical applications of sugar-based contrast agent studies in the brain, cancers, stroke, and Alzheimer's disease (AD). Challenges and opportunities associated with using sugars in clinical imaging are described in Section 6.[40]

2. PHYSIOLOGICAL PROPERTIES OF SUGAR ANALOGUES

Figure 1 gives a summary of sugars that have been studied at present using exchange MRI (Fig, 1A). Not surprisingly, the first sugars studied as contrast agents *in vivo* were D-Glc,[29,30,41–54] and other single-ring hexoses, such as 2-deoxy-D-glucose (2-DG),[55,56] 3-o-methyl-D-glucose (3-OMG),[57–60] and D-glucosamine (D-GlcN).[61,62] Some artificial sweeteners (sucralose, Slc, and maltitol, Mlt) and glucose dimers (Maltose, Mls) and polymers (dextrans, dex) have also been investigated. Of all of these, until this year, only D-Glc had been studied in humans,[45–48,52–54,63–66] the reason being that it is already approved as a drug for intravenous glucose tolerance testing. A simple three-compartment model[41,67,68] can describe the biodistribution of sugars in most tissues: (1) vasculature (*v*), (2) extravascular extracellular space (EES, (*e*)) and (3) intracellular (*c*). As an example, the characteristics of tissue delivery, uptake and metabolism of the above sugars in tumors are shown in Fig. 1B. In other tissues, additional parameters may have to be accounted for, especially the BBB for transport into the brain, and the predominance of aerobic metabolism in most cell types in healthy tissue. From a simple organizational point of view, to understand the imaging findings in terms of compartmental signal origin, we can separate the sugars in four types: (i) Sugars transported into the cell and fully metabolized (D-Glc), (ii) those that are taken up and, within the period of dynamic contrast measurement, phosphorylated only (FDG, 2-DG, D-GlcN, GlcNAc), (iii) those are just taken up and

accumulate within the limited scan period (3-OMG and xylose), and (iv) those that, similar to GBCAs, are not transported into the cell (L-Glc, Slc, Maltitol, Mls, dextrans).

2.1 D-Glc

D-Glc is the natural substrate for most tissues. After delivery and facilitated transport into the cell, it undergoes glycolysis to pyruvate, which is further metabolized aerobically in the tricarboxylic acid (TCA)-cycle to glutamate, glutamine and other derivatives.[69,70] Under ischemic conditions, anaerobic glycolysis is activated with the end product being lactate. Despite the availability of millimolar amounts of substrate, the concentration of phosphorylated glucose products and pyruvate in the cell are in the micromolar range,[71] which currently is too low to be detected by MR, indicated by a white color in Fig. 1B. In the healthy cell, the total amount of glutamate is constant,[72] and no signal change is expected in the MR spectrum. Lactate accumulates during tissue ischemia or in actively metabolizing tumors, but the OH group of lactate resonates very closely to water and is not easily detectable in CEST, CESL or CE-T_2 relaxation experiments at clinical field strengths. Therefore, the main signal from D-Glc originates from the vasculature and the EES, which in case of a lack of a tissue barrier (BBB or other) will have the same concentration of D-Glc concentration. The reason the EES has a darker indication for more signal in Fig. 1B is that the pH in the EES of tumors is lower than in blood due to lactate exported from the cell. Because OH exchange for sugars is base-catalyzed in the physiological range (above pH = 6),[73,74] the exchange rate reduces with increased acidity. As OH exchange is very fast on the MR timescale, OH signal is merging with the water signal in the Z-spectrum. The reduced pH edges the OH protons to a slower exchange regime,[75] leading to increased detectability at lower pH for these fast exchanging protons (see Section 3 and Fig. 2C for an illustration of the effect of pH changes on the water saturation in the presence of a sugar contrast agent). In normal blood, the D-Glc concentration is about 5 mM and in intravenous (i.v.) DGE studies in humans, this is elevated to about 10–20 mM, depending on the amount (typically about 25–35 grams)[77] and timing of infusion and the insulin response. D-Glc is considered safe and has regulatory approval for other purposes (e.g. i.v. glucose tolerance testing,[78] which has led to enthusiasm in the CEST field for using D-Glc as an alternative to FDG-PET. However, as shown in Fig. 1B, the D-Glc signal origin is different from FDG and its uptake signal includes the sum of delivery, transport and phosphorylation. Unfortunately, there is only a single signal to be studied and separation into the different contributions is not trivial. On the other hand, some recent applications, e.g., in AD models (see below) are showing promises[79,80], and the field has to be further developed to understand the possible applications.

2.2 FDG and 2-DG

Contrary to D-Glc, the metabolic pathways of 2-DG and FDG[41,49,55,81] stop after the first step of glycolysis (phosphorylation), after which 2-DG-6-phosphate (2-DG-6P) and FDG-6P are trapped intracellularly (Fig. 1B), which provides a long imaging window.[49,55,56,81–83] Therefore, by measuring their accumulation over a prolonged period of time thus removing the influence of delivery and transport (generally one hour in FDG-PET), these sugar products can be used as an indicator of glucose metabolism.[49,55,56,81–83] Because of the glycolytic inhibition property of these sugars, they have been considered as a drug for

cancers.[84–86] Unfortunately, these deoxyglucose analogues are toxic with LD50 of 8 g/kg in mouse i.v.[87]

2.3 D-GlcN and GlcNAc

D-GlcN and GlcNAc are amino monosaccharides that are transported into the cell via the glucose transporters GLUT1 (same affinity as D-Glc) and GLUT2 (~20 times more affinity)[88]. Once in the cell, these sugars are phosphorylated and slowly metabolized.[89–91] As a consequence, GlcN-6P and GlcNAc-6P will accumulate in the cell making them a useful contrast agent, especially for tumor cells where they are often overexpressed. Rivlin and Navon[61,62] therefore suggested that these are good agents for human study, especially in view of their low toxicity (both per os (P.O.) and i.v.[92,93]). They are also available over the counter as a nutritional supplement, as well as a drug for treatment of osteoarthritis[94] and inflammatory bowel disease.[95] Rivlin et al. also pointed out that high oral doses (5–15 g/kg P.O.) are well tolerated in humans[89,96] and that concentrations over 10 mM can be produced a few hours after oral administration, with a half-life time of many hours.[89,96,101] This long time window and the fact that neither D-GlcN nor GlcNAc show significant effects on blood insulin and glucose levels,[97] making them very suitable even for diabetic populations.[98] Both compounds also cross the BBB.[99,100]

In an exciting recent first human study, using a dose of 7.5g GlcN-sulfate in 150 mL per person, Rivlin et al. demonstrated the possibility of D-GlcN to highlight breast tumors.[101]

2.4 3-O-Methyl-D-Glucose (3-OMG) and D-xylose (D-Xyl)

3-OMG has a similar transport mechanism as D-Glc but cannot be phosphorylated by hexokinase. Therefore, it can be used as a substrate for studying glucose transport into the brain and tumors[58–60,102,103] and since it accumulates after transport, to identify the location of tissues with increased uptake.[57] A typical dose of 3-OMG to study nutrient absorption has been 30 mg/kg in pediatric patients[104] and up to 2.5 g in adult.[105] 3-OMG is in general regarded as non-toxic, as it is not phosphorylated. It was found that it plays a role in regulating the thioredoxin-interacting protein.[106] The typical allowed dose for D-glucose is 500 mg/kg[77] and has been used up to 35 g in adults.[107] In animal studies, when given at the same concentration as D-Glc, 3-OMG showed an approximate doubling of contrast.[59] Therefore if 3-OMG is to become a useful contrast agent it has to be proven that it can be given at a higher dose than in previous human studies, i.e. close to that of D-Glc.

Recently, xylose (D-Xyl), a plant sugar that has been used as a diabetic sweetener in food products, was added to the list of potential exchange-based agents by Wang et al.[108] It has transport properties similar to D-Glc, but minimal metabolism in human tissues including the brain.[109,110] It has already been approved by the Food and Drug Administration (FDA) for human use at a dose of 25 g P.O. in malabsorption testing[111] and at doses of up to 1.5 g/kg in children. Combinations of 25 g P.O. and 10 g i.v. infusions have also been used.[111,112] While inducing an insulin response, D-Xyl barely affects blood glucose levels and actually has shown some benefits in regulation blood glucose levels in patients with diabetes.[113,114] Xylose can be transported across BBB, and was detected in rat brains using an on-resonance spin-lock approach[108]. Based on the lack of metabolism in brain, we added

D-Xyl in the same row as 3-OMG in Fig. 1B, but we could not find any literature on D-Xyl in tumors to verify this.

2.5 L-Glc, Slc, Maltitol, D-Maltose and dextrans

L-Glucose (L-Glc) is an enantiomer of D-Glc[49] that cannot be metabolized. L-Glc transport *in vivo* differs from D-Glc in that it is transported across the placenta less actively[115], while transport across the BBB was found to be less than even for the polymer inulin.[116] It is taken up only in tracer amounts by cancer cells.[117,118] Using CESL and CEST, L-Glc contrast could not be detected in the brain.[49,55] As such, it has been used in animals to evaluate the BBB leakage in brain tumors.[49,55] Physiologically, it decreases hematocrit and blood viscosity.[119] Thus, any interpretation of the dynamical changes caused by L-Glc should be cautious in view of these physiological effects of L-Glc. It should also be mentioned that L-Glc has a laxative effect and has been used as a colon-cleansing agent in adults before colonoscopy (24 g in 8 oz of water).[120] This is not optimal for use as a contrast agent.

Slc (Splenda) and maltitol are artificial sweeteners that have been tested as exchange agents by Bagga and coworkers.[121,122] They are safe for their intended use as sweeteners[123]. Slc could reduce or perturb the intestinal microbiota[124,125] and have other metabolic effects.[126] Similarly, maltitol could have an effect on gastrointestinal microbiota.[127] Further investigations on their physiological effects other than their intended use could help to navigate their potential imaging applications in humans.

The glucose polymers D-maltose[18] and dextrans[32,34,35,129] have also been suggested as exchange-based contrast agents. D-Maltose is a 1–4 linked disaccharide that is not taken up or metabolized by the cell.[18] Dextrans are 1–3 or 1–6 linked polymers of glucose that cannot be transported or metabolized by mammalian cells. While limited studies were found related to D-maltose, it could lead to an increase in specific extracellular enzymes, such as glucoamylase.[129] High molecular weight dextrans have been used in clinical studies for several decades with an excellent safety profile.[130] Both dextran-70 at 6%, 4 mL/kg and low molecular weight dextran-1 are safe, which have been used widely for hypersensitivity inhibition and islet autotransplantation in children.[105,131] Despite some risk for anaphylaxis for larger size molecules, dextrans have a long established safety profile which could be promising for repurposing them as contrast agents in humans.

These compounds do not cross the BBB and are generally not metabolized by mammalian cells and as such are expected to be excellent substitutes for GBCAs for the goal of studying tumor enhancement, BBB breakdown and even angiography. Except for L-Glc, they have low toxicity and are expected to be suitable for both oral or i.v. delivery.

3. MR SPECTRAL PROPERTIES OF SUGAR ANALOGUES

The hydroxyl resonances of cyclic hexoses such as D-Glc (Fig. 2A) and its analogues (2-DG, 3-OMG, D-GlcN, GlcNAc) can be visualized in NMR spectra for solutions in H_2O at low pH and low temperature, such as shown at 11.7T for D-Glc in Fig. 2A and 3-OMG in Fig. 2D. The exchangeable proton resonances of the two enantiomers in solution (e.g. for D-Glc in Fig. 2B) appear over the approximate ranges of 0.6–0.8 ppm, 1.1–1.7 ppm,

2.1–2,2, and 2.8–2.9 ppm relative to the water resonance assigned to 0 ppm for reference (Figs. 2A, D). For glucose polymers with linkage in the 1-position or analogues without a hydroxyl group in the 1-position, the spectral range is generally limited to the 0.5 – 1.8 ppm range. Increasing the temperature (Fig. 2A) and the pH and buffering the solution will make these resonances invisible in the ^{1}H NMR spectrum due to exchange broadening, but they remain visible in the water saturation spectrum (Z-spectrum, Fig. 2C). At low pH in PBS (Fig. 2C), these Z-spectra[36,41,42,49,51,56,57,59–62,81–83,102,103,132] show similar ranges for the resonance maxima as the NMR spectra, but these saturation signals are broadened and appear to be pushed to higher frequency when increasing B_1, an effect due to the interfering effects of direct water saturation and, *in vivo*, the semi-solid magnetization transfer effect. Not unexpectedly, based on the number of protons involved, the maximum signal appears around 1.2 ppm for most glucose analogues which has become a popular offset frequency to be used in DGE experiments (see below). When increasing the pH to physiological levels, all signals start to merge with the water resonance due to faster exchange (Figs. 2C, E). Even at the high field of 14.1T the spectrum is in the intermediate exchange regime: $\Delta\omega\ rad/s \approx k_{ex}\ (Hz)$, while it moves closer to the fast exchange regime at clinical field strengths such at 3T. Thus, under physiological conditions, the hydroxyl protons of sugars are typically detected over the 0–2 ppm range in the Z-spectrum, with features depending on pH and the static field strength B_0 and the RF strength B_1 used. *In vivo*, the Z-spectrum is complicated with potential contributions from other hydroxyl protons, for instance from glycogen[36] present at high concentration in liver and muscle, or myoinositol in the brain.[133] Other exchangeable protons, e.g. from amine protons in glutamate in the brain[134] may also contribute. Fortunately, when using sugars as contrast agent, we study the dynamic difference time curve of the Z-spectrum and these other interfering resonances can be (partly) subtracted out. As seen above from Fig, 1, different sugars have specific transport and utilization *in vivo*, so they can reflect different physiology or pathology when used as unique CEST contrast agents. Moreover, the sensitivity of the Z-spectrum to exchange rate may be exploited to better visualize pathological microenvironments, such as the acidic tumor microenvironment (EES ~pH 6.5–6.8) where the fast exchanging hydroxyl protons slow down, increasing their detectability in tumors.

4. METHODOLOGY

4.1 Exchange sensitized acquisition

The exchange rate k_{ex} of the hydroxyl protons in D-Glc or its derivatives under physiological conditions is more than 3 kHz (Fig. 2E) and in addition to using chemical exchange label transfer, sugars also reduce the water proton transverse relaxation time, T_2.[13,17,135] This mechanism, which also underlies the CESL technology, is based on signal dephasing due to exchange between the frequency of the solute proton and the water frequency (see below for the equations). Exchange-based contrast has been obtained by either the acquisition of Z-spectra or by dynamic-glucose enhanced MRI,[136] where typically signal intensities at specific offset frequencies related to sugars are acquired at a temporal resolution of a few seconds or slower, depending on the number of slices and the image resolution. Any pulse sequence that is designed to be sensitive to exchange transfer (CEST, CESL) or T_2 relaxation can be used for DGE MRI. Numerous approaches, including both

off-resonance and on-resonance, have been investigated (see Fig. 3 for some examples), with the “on-resonance” terminology relating to the water proton frequency. CEST with full Z-spectral acquisition is the most suitable technique for both static and dynamic acquisitions since it may offer some distinction of contributions based on chemical shift and allows frequency referencing to correct for possible B_0 changes due to field drift or subject motion. The on-resonance techniques are only suitable for dynamic studies since no chemical shift information is encoded. The field strength (B_0) and saturation parameters (B_1, pulse shape and length, inter-pulse timing) dictate the detection sensitivity of D-Glc and its analogues *in vivo* (Fig. 2).[75]

A key difference between DGE approaches and studies designed to detect endogenous exchangeable species is that the CEST contrast agent (glucose or its derivatives) is given intravenously during the MRI scan. The change in signal can therefore be attributed to the effect of the injected contrast agent. In most studies, quantification of DGE signal is performed by taking the difference between post-injection scans at each time point and the average of the pre-injection scans, followed by analyzing the dynamic time difference curve. The first DGE studies used classical saturation transfer parameters, namely long, low B_1 off-resonance RF irradiation (continuous wave, CW; or pseudo continuous wave) lasting between 1–2 s. Contrary to classical CEST MRI, where the irradiation frequency is changed, a single fixed irradiation frequency was used in early DGE MRI studies to allow the detection of dynamic signal changes with higher temporal resolution. As mentioned above, since there is an expected signal maximum around 1.2 ppm at lower pH and all signals merge at higher pH, it has been common to use this frequency offset. A few DGE studies at ultrahigh fields (11.7T, 9.4T and 7T) used this approach.[44,45] At lower field strength, such as 3T, the frequency separation between protons at 1.2 ppm and bulk water becomes smaller (~150 Hz) and saturating at this frequency will result in profound direct water saturation effects. In addition, a signal coalescence effect of hydroxyl protons with water protons occurs due to being in the intermediate to fast exchange regime, which removes any frequency specificity for the hydroxyl protons. Fortunately, all exchangeable protons downfield of water collectively still result in an asymmetry of water spectrum.[53] Figure 4 illustrates this effect at 7T and 3T. Under such conditions, it is no longer crucial to set the irradiation frequency at 1.2ppm and an offset judged on a trade-off between maximal CEST signal and water direct saturation can be determined for the B_1 used. An initial *in vivo* human DGE study at 3T used a frequency offset of 2 ppm.[53] The use of a single frequency instead of asymmetry analysis makes the signal change sensitive to symmetric changes in the water signal after injection, such as a change in T_2 or T_1. T_1 does not change upon infusion,[17] but T_2 decreases enhance the DGE effect. Possible changes in S_0, e.g. due to magnetic susceptibility changes or water content changes affect the results of both approaches. In the current literature, the effects of these contributions have not yet been analyzed.

An alternative way to avoid the coalescence effect while at the same time sensitizing to rapid chemical exchange is to use on-resonance techniques.[137] The on-resonance CESL technique (Fig. 3B) has been used both in pre-clinical[43,49,58] and human studies at various magnetic fields.[46,47,52] During the spin-locking period (TSL), the decay of the water signal is governed by the T_1 relaxation rate in the rotating frame, $R_{1\rho}(1/T_{1\rho})$. The presence of fast

exchanging protons with a frequency different from water protons will increase the R_2 and $R_{1\rho}$ due to exchange-mediated signal dephasing:[17,43]

$$R_2 = R_{2,0} + R_{ex} \quad [1a]$$

$$R_{1\rho} = R_{eff} + R_{ex}^{SL} \quad [1b]$$

In the case of on-resonance spin lock, $R_{eff} = R_{2,0}$, where $R_{2,0}$ is the transverse relaxation rate of water protons without chemical exchange contribution; R_{ex} is the exchange induced relaxation rate. Assuming a proton pool at a single offset and that the exchange effect of the administered sugar will dominate the change in relaxation, the changes in R_2 and in on-resonance $R_{1\rho}$ upon glucose injection can be expressed as:[17,43,138]

$$\Delta R_2 = \Delta R_{ex} + \Delta R_{2,0} \approx \Delta R_{ex} = \frac{\Delta p \cdot k_{ex} \cdot \Delta\omega^2}{\Delta\omega^2 + k_{ex}^2} \quad [2a]$$

$$\Delta R_{1\rho} = \Delta R_{ex}^{SL} + \Delta R_{2,0} \approx \Delta R_{ex}^{SL} = \frac{\Delta p \cdot k_{ex} \cdot \Delta\omega^2}{\Delta\omega^2 + \omega_1^2 + k_{ex}^2} \quad [2b]$$

where Δp is the ratio of hydroxyl proton concentration of the exogenous agent to water proton concentration, k_{ex} is the exchange rate (in Hz) and $\Delta\omega$ is the chemical shift between the hydroxyl protons and water protons (in rad/s). $\omega_1 = \gamma B_1$ is the amplitude of the spin lock field (in rad/s). Notice that the rotating frame exchange-based relaxation enhancement increases with reduced spinlock field to the limit of being equal to the transverse relaxation rate change without RF irradiation. When measuring a spin-lock based Z-spectrum, the observed signal change needs to be normalized to the signal without spin lock preparation. The normalized relative signal change can be approximated as: $\Delta S_{rel} \approx \Delta R_{ex} \cdot TSL$, and given a fixed spin-locking time (TSL), the signal is proportional to change in exchangeable proton concentration, Δp.[64]

When comparing detection sensitivity between CEST enhancement (~ $\Delta p \cdot k_{ex} \cdot \alpha$, in which $\alpha \approx \omega_1^2/[\omega_1^2 + k_{ex}^2]$) and the relaxation enhancements, it is important to note that all methods have a proportionality to $\Delta p \cdot k_{ex}$. This is multiplied by a method-specific ratio that is 1 or less, which includes MR acquisition or spectral parameters (e.g. RF strength and chemical shift difference). Thus maximum effect size should be similar between these approaches. These latter terms can be used to optimize sensitivity with respect to acquisition or agent properties for ω_1^2 and $\Delta\omega^2$ respectively. Depending on the agent, the relative magnitude of these terms versus the exchange rate determines the enhancement. Notice that while CEST signal can be optimized with B_1, the relaxation methods have an inherent B_0 dependence in the term $\Delta\omega$, which leads to optimal detection of D-Glc under physiological conditions at a field strength about 11.7T (~ 5 times larger signal than at 3T)[17]. In addition, when studied at the D-Glc frequency between 1–2 ppm, the Z-spectral changes during the first few minutes in the dynamic scan should be specific for D-Glc and include an additional effect due to the transverse relaxation rate increase.

An issue with ultra-high field human scanners (≥7T) is the presence of strong B_1 and B_0 field inhomogeneities. Using conventional hard 90° pulses for the flip-down flip-up pulses surrounding TSL can cause severe image artifacts and reduced locking efficiency due to a mismatch between the excited magnetization and the spin locking field. Therefore carefully designed adiabatic pulses that are immune to B_1 field inhomogeneities are important for *in vivo* DGE studies at ultra-high field.[64]

Another technique that has been used in DGE studies is the on-resonance variable-delay-multi-pulse (onVDMP) method (Fig. 3C),[139] composed of a train of binomial pulses interleaved by short delays. The term "variable delay" stemmed from the original off-resonance version of the sequence, a special version of the frequency-labeled exchange (FLEX) transfer method,[140,141] where the mixing time (delay) between saturation periods was varied to serve as an exchange rate filter.[142,143] Since fast exchange causes the frequency label to transfer rapidly during the mixing time, the delay between pulses can be as short as possible within specific absorption rate limit.[144] The signal resulting from the onVDMP sequence is:

$$S = S_0 e^{-t_{on} R_{on}} \quad [3]$$

where t_{on} is the length of the onVDMP pulse train; R_{on} is the relaxation rate during onVDMP which is sensitive to exchange, which can be described using relaxation theory.[145] The R_{on} is very similar to $R_{1\rho}$ except that the water magnetization is being kept predominantly along the longitudinal direction by the binomial pulses.

With glucose infusion:

$$S + \Delta S = S_0 e^{-t_{on}(R_{on} + \Delta R_{on})} = S \cdot e^{(-t_{on} \cdot \Delta R_{on})} \quad [4]$$

the normalized signal change is:

$$\frac{\Delta S}{S} = e^{(-t_{on} \cdot \Delta R_{on})} - 1 \quad [5]$$

When $-t_{on} \cdot \Delta R_{on} \ll 1$, this can be approximated as:

$$\frac{\Delta S}{S} = -t_{on} \cdot \Delta R_{on} \quad [6]$$

Similar to on-resonance spin lock technique, the onVDMP method provides higher sensitivity in detecting glucose signal[146] and is sensitive to B_0 and B_1 field inhomogeneities. The latter can be mitigated by using a simple phase cycling scheme.[79,80] Inverting the phases of some binomial pulses improves the robustness of onVDMP against small shifts in water resonance frequency and B_1 inhomogeneity as demonstrated by a recent report.[80] At ultra-high magnetic field, onVDMP DGE imaging showed improved signal sensitivity compared to CW-CEST,[146] and equivalent sensitivity to onCESL.[80]

It is important to point out that while exchange sensitive on-resonance techniques detect all fast exchanging protons, this lack of specificity is generally not an issue with DGE experiments since the sugar is given as a contrast agent. The change in signal that is detected following the injection can be attributed to the change introduced by glucose (concentration, pH, osmolarity and eventually metabolism). It might be worth noting that in the later part of the DGE dynamic curve (>5 min), the signal may have contributions from D-Glc metabolic products, such as lactate in tumors. Some rapidly exchanging products may contribute more weighting in onVDMP and onCESL images than in CW-CEST images.

T_2 relaxation can also be exploited to detect the change in sugar concentration.[13,17,135,136] Standard fMRI techniques such as blood oxygen level-dependent (BOLD) MRI can be used to detect changes in certain regions of the brain following oral glucose intake or IV glucose injection.[107,147] A T_2 specific measurement for DGE would use a Carr-Purcell-Meiboom-Gill (CPMG) pulse train (Fig. 3D), which employs of a series of refocusing 180° pulses to preserve T_2 effect while reducing the effect of inhomogeneities. When used as preparation, the refocusing series is surrounded by two 90° pulses of opposite phase. A very recent paper compared the CPMG, onVDMP and onCESL in a single DGE session in a mouse study.[19] The CPMG method showed the highest change of DGE signal in brain parenchyma upon glucose infusion, but showed high level of fluctuations in signal in the CSF, most likely due to through-plane flow.

When choosing a suitable technique for DGE experiments, considerations need to take into account magnetic field strength, inhomogeneities of the B_0 and B_1 fields, the targeted anatomy (eg. brain parenchyma vs CSF), length of the dynamic study, hardware and SAR limitations, and for clinical scanners, sequence availability.

4.2 Quantification

Analysis of static Z-spectra for sugar studies is similar to that for other fast exchanging compounds[75] and not discussed here. For dynamic studies, the quantification of the DGE hemodynamics has some resemblance to tracer kinetic contrast agent methods, but several important details are different. Firstly, glucose is not really a tracer due to the large quantity that gets injected. Secondly, the infusion period is much longer than what is used typically for other contrast agents (e.g. 1–4 minutes for glucose compared to 3–4 seconds for GBCA). While DGE is being further established, investigators have used some simple approaches to at least get an impression of how the signal is changing. A common one is to calculate the area under the curve (AUC) of the DGE signal response, either by normalizing the signal to S_0 or to the average baseline signal (S_{base}) and then subtracting the measured signal at each time point from this normalized reference signal. This difference signal is then integrated:[44,45,48,53,59]

$$AUC = \frac{1}{n}\Sigma_1^n \frac{S_{base}}{S_0 \quad or \quad S_{base}} - \frac{S(t_n)}{S_0 \quad or \quad S_{base}} = \frac{1}{n}\Sigma_1^n \frac{\Delta S(t_n)}{S_0 \quad or \quad S_{base}} \qquad [7]$$

To compare between studies or time periods of integration, the signal difference can be normalized based on the number of acquisitions (n). Challenges in kinetic modelling of

DGE MRI are not only related to the large volume injected and the slow infusion. Contrary to Gd agents, D-Glc is transported over the BBB and blood CSF barrier in normal tissue. The main issue for quantitative analysis then is the availability of only a single exponential-like tissue response curve that reflects the convolved effects of D-Glc delivery, tissue uptake and metabolism. The theory for this effect has been described previously for ^{13}C-glucose uptake studies using a rapid hyperglycemic clamp in which blood D-Glc was ramped to maximum within a minute and kept constant, basically providing a rectangular arterial input function (AIF)[143] to simplify the analysis.[68] There have been some disagreements on whether intracellular phosphorylated glucose compounds contribute, but older literature has shown that their concentrations are in the micromolar range in normal tissue and not relevant as a signal contribution.[68] Also, the D-Glc concentration reduces per transport step with a factor of 4–5, i.e. from blood to EES and from EES to intracellular. In tumors, when the BBB is leaky, the EES concentration will be comparable to that in blood, but the intracellular concentration decays fast[148] due to fast metabolism[41] (Fig. 1B). Another potential issue is that in tracer kinetic modeling one usually has to convert signal to concentration. While D-Glc CEST signal and thus CEST-based DGE signal changes have been confirmed to be proportional to concentration (Δp term in the equations above) in phantoms, such a conversion is complicated at higher concentrations (> 20–30 mM) and higher B_1 values as water saturation becomes limited due to back exchange of saturated protons. Furthermore, *in vivo* factors such as pH differences between tissue compartments, competing background magnetization transfer effects, as well as contributions from changes in the transverse relaxivity of D-Glc due to OH proton exchange.[13,17] For the relaxation methods, proportionality to concentration should extend to higher concentrations. Another difference from conventional contrast agent methods is that the response to D-Glc may vary between individuals due to differences in insulin response and glucose metabolism.[48] Thus, AIF measurements resulting from the DGE experiments cannot be generalized and the retrieval of individual AIFs will probably be needed to quantify hemodynamic parameters.

5. APPLICATIONS

Exchange-based imaging of D-Glc and its analogues provides an approach to study alterations in glucose uptake and utilization, in particular in the brain where D-Glc transport and metabolism are tightly regulated and abnormalities could indicate pathological status. Moreover, the exchange-based signal is dependent on the tissue environment, especially pH, that may be affected under specific physiological and pathological conditions. For example, tumors have an acidic pH in the EES, leading to higher exchange-based effects as the exchange rate slow-down allows more efficient labeling. Many interesting studies in cancers, stroke, Alzheimer's disease, placenta and kidney have been published, especially in animals, but also in humans. Currently published exchange-based studies using D-Glc, 2-DG, and 3-OMG are summarized in Table 1, which includes animal models, field strength, pulse sequence and acquisition method used, as well as the frequency offset employed for dynamic scans.[19,41–56,64–66,79–83,108,146,150–153] Due to the abundance of studies, we will just give a few examples that should be representative of current options and capabilities for physiological studies.

5.1 Cancer

D-Glc is a primary source of energy for cells and a precursor for the synthesis of various important metabolites. Tumors, such as gliomas, prostate and breast carcinomas have a high reliance on anaerobic glycolysis and display a concomitant increased production and cellular export of lactate, which results in a decreased pH in EES.[155] Moreover, leaky vasculature and upregulation of the glucose transporters GLUT1 and GLUT3 may also occur as a consequence of aggressiveness.[5]

GlucoCEST contrast was first demonstrated in two independent studies in tumor mouse models after administration of D-Glc.[41,42]. In a study of a mouse breast tumor models, a lower glucoCEST contrast was observed in MDA-MB-231 tumors compared to MCF-7 tumors, which was explained tentatively by the authors to be due to the higher utilization of glucose in the aggressive tumors (MDA-MB-231),[41] which in view of the below considerations may not be correct. Interestingly, differences between these two tumors were not observed in FDG-PET and contrast-enhanced MRI, leading to the conclusion that different mechanisms of contrast play a role. In the other early study, Walker-Samuel et al.[42] demonstrated that glucoCEST could distinguish two types of colon tumors (LS174T and SW1222). These results correlated with FDG-PET uptake findings. However, correlation need not imply causality. Based on the different signal origins for D-Glc and FDG (Fig 1B) and the low concentration of phosphorylated glucose derivatives in tumor cells, it should be kept in mind that PET and glucoCEST provide intrinsically different information.

A great advantage of exchange-based MRI over MRS is that it allows acquisition at a higher spatial and temporal resolution, allowing the acquisition of dynamic data similar to those when using GBCAs. As a first example, DGE MRI using D-Glc has been shown to generate valuable information about D-Glc uptake kinetics in the brain and brain tumors. A first study of mice with glioblastoma[44] showed that the dynamic curves could clearly distinguish tumor from healthy tissue both in terms of maximal signal intensity and AUC, similar to DCE results in the same animals. The differences between tumor and contralateral normal brain in DGE reflect the perfusion properties and BBB breakdown[43–45] and the enhanced tumor signal were attributed to the relative low pH microenvironment of tumors (~6.5–6.8 pH) and high blood volume in tumors (Fig. 1B). To understand this, it is important to know that the intracellular concentrations of D-Glc and its phosphorylated products have been reported to be negligible (micromolar concentrations) in tumor cells[156] and the brain[68] and that lactate is not well detectable with CEST, especially at frequencies above 1ppm. So fast metabolism to lactate should not increase the DGE signal but actually delay reaching its maximum and further lead to reductions when substrate runs out. A recent study by Jin et al.[49] using multiple sugar monomers provides important insight into the signal origin for DGE studies and great support for the principles outlined in Fig. 1B. They compared DCE using GdDTPA (Fig. 5A) with DGE curves for D-Glc, 2-DG and L-Glc at the same infusion concentration (Fig. 5B) for a rat 9L glioma model. The results in Fig. 5B, show several relevant features. (i) the D-Glc and L-Glc peak maxima at about 4–5 min (Fig. 5B) are equal within error. This is experimental confirmation that most of the CESL-MRI signal comes from the EES due to low concentrations of intracellular sugar and its phosphorylated products (see above[69, 156,157]). As L-Glc is not preferentially

transported by GLUT,[49,56] its signal increase after infusion is a good indicator of that in EES and vasculature after BBB breakdown (cf. Fig. 1B). This is further confirmed by the time curves of DCE and L-Glc based DGE being comparable within error (Figs. 5D, E). (ii) the D-Glc curve increases slightly slower than the L-Glc curve (Figs. 5B,D), which we attribute to transport into the cell and metabolism; (iii) the maximum CESL ($\Delta R_{1\rho}$) signal change for 2-DG infusion is several times that of D-Glc (Fig. 5B)[49], attributed to signal from the intracellular accumulation of 2-DG-6P (cf. Fig. 1B) adding to that of vasculature and EES; (iv) the D-Glc signal decreases at later time points (Fig. 5B), attributed to continuous metabolism by the tumor to lactate, a metabolic product not easily detected by CESL[49] or CEST at low field,[29] due to a small chemical shift difference with water. Overall, the results of Jin et al.[49] confirm the principles outlined in Fig. 1B, but these authors are also careful to point out that the relative contribution in the EES may be higher for CEST than for CESL because CESL is less sensitive to pH changes. The same study of Jin et al.[49] also showed a small uptake of L-Glc in contralateral brain (Fig. 5C), presumed normal, on which the authors did not comment, but which we attribute to contributions from blood vessels in the voxel. Contralateral brain showed reductions in 2-DG and D-Glc uptake by a factor of about two (Fig. 5C) relative to tumor (Fig. 5B). In this case, L-Glc should be due mainly to blood vessels and D-Glc to vessels + EES. However, compared to tumor EES, normal brain EES has reduced D-Glc concentration (about 1/4 of the blood value[61]) due to facilitated transport over the BBB. This is also most likely one of the causes of the uptake curve of D-Glc in normal brain being slower than in the tumor (Fig. 5F), but not the only one as the half-time of D-Glc uptake into the brain is about 1–2 min[68,158,159]. Actually, the maximum of the DGE curve has moved to about 15 min, possibly due to the contribution of glutamate metabolism, which is being produced on this time scale. The fact that the uptake signal in normal brain is not a factor of 4 less could be due to contributions of the metabolic products of the TCA cycle (glutamate, glutamine) contributing to the non-specific on-resonance CESL and on-resonance VDMP signal, but in general these are turned over and maintained at constant levels in the brain[160–162]. So the reason for this factor is less clear, and will have to be investigated further.

Among a few other studies that have also investigated the compartmental contribution of glucoCEST signal,[56,151] DGE was recently used to study D-Glc utilization changes under the glucose deprivation treatment (mTOR inhibitor) in a mouse glioblastoma tumor model. With minimal intracellular contribution due to the inhibition of hexokinase activity by mTOR, the DGE contrast increased under the treatment, which supports the notion that DGE detects the accumulation of glucose in the vascular and EES compartments (Fig. 1B).

Dextran is a clinically used natural polysaccharide that is a polymeric form of glucose. It is available in multiple molecular sizes (5.9 nm – 77.0 nm),[32] and each dextran particle has a high number of hydroxyl protons. Liu et al. have demonstrated that dextrans of molecular weight ranging from 10 kD to 2000 kD generate CEST contrast at 0.9 ppm.[32] The Z-spectrum of dextran also showed a different T_2 contribution compared to D-glucose solution, which could be attributed to the different exchange environment in forms of particles. Dextrans of different sizes have been used to characterize the vascular permeability of different tumor regions (Figs. 6A–C),[32] by injecting a low-molecular weight (10 kD) dextran first (t = 0) and a heavier (70 kD) after clearance of the first (t = 40 min). The 70 kD

agent occupied a tumor area similar to a Gd-enhanced study of the same rat, while the 10 kD agent showed penetration over a larger area. In another study,[34] this high molecular weight dextran was used to monitor vascular disruption therapy. The same group used dextran with an added prostate specific membrane antigen (PSMA) targeting ligand to show promise in identifying tumors with high PSMA expression ($PSMA^+$, PC3-PIP cells) through selective retention as a function of time.[31] This is illustrated in Figs. 6D,E, where the contrast in PSMA overexpressed and control ($PSMA^-$, PC3-flu cells) tumors initially had comparable contrast (Fig. 6E), which changed to only PSMA+ tumors being highlighted at longer time points.

Multiple sites have implemented DGE MRI for assessing brain tumor patients at 3T and 7T, with both glucoCEST[45,53] and glucoCESL[46,47,52,64,66] being applied. Interestingly, DGE maps showed partly similar enhancement in tumors when compared with DCE-MRI using GBCAs. Due to the difference in the compartmental contributions in DGE vs DCE, other than BBB permeability, DGE may provide useful and unique information to indicate key events in tumors, such as altered glucose uptake, perfusion and metabolism, for cancer diagnosis/staging, follow-ups and monitoring treatment response. In the consideration of compartmental contrast and cancer pathology, imaging sugars enables the assessment of glucose uptake and utilization in both tumor regions and normal brain regions,[19,34,44–46,49,52,54,64,66,150,163] where glucose is transported and metabolized. FDG-PET mainly detects the elevated glucose uptake in tumors. GBCA DCE-MRI detects the BBB breakdown in tumors. The unique information provided by the DGE MRI uptake signal in terms of the delivery, transport and metabolism of D-Glc may facilitate the assessment of different types of cancers, especially in non-Gadolinium-enhancing brain tumors.

5.2 Alzheimer's disease

Alzheimer's disease (AD) is a progressive neurodegenerative disease that leads to neuronal cell death and brain atrophy. Early pathology includes glymphatic dysfunction, hypometabolism and hypoperfusion.[83,164–168] Plaques will then be formed by two well-known mechanisms related to beta amyloid and tau proteins.[169] Moreover, reduced glymphatic clearance was found to associate with the formation of plaques in AD.[170–172]

CSF forms a major part of the glymphatic system (Fig. 7A), Huang et al. and Chen et al. recently developed a DGE method using onVDMP to detect glucose in both the CSF and parenchyma[79,80] to facilitate the assessment of glymphatic system in AD. Huang et al., using a mouse model of amyloid plaques (APP/PS1) at 3T, reported a three-fold decrease in the glucose clearance (μ_{out}) in CSF of young (6 months old) AD mice compared to age-matched wide-type mice[100] (Fig. 7B), while little or no observable plaques were found in the brain. This reduced clearance was also observed in the cohorts of old mice (16 months old, Fig. 7B). Moreover, the glucose uptake maximum signal (S_{max}), which is the convolved signal increase due to effects of delivery, transport and metabolism, was lower in old AD mice compared to young AD mice (Fig. 7B). In the parenchyma, an increase in the rate of glucose uptake (μ_{in}) was observed in old AD mice (Fig. 7C) compared to young AD mice. Interestingly, this was not observed in the WT cohorts, which may provide essential

parameters for the identification of AD from normal aging. Another point to note is that the measured μ_{in} of WT parenchyma from this study was comparable with the D-Glc uptake rate measured by van Zijl et al. in the cat brain using ^{13}C MRS.[68] These results indicate that DGE MRI generates multiple parameters to detect changes of both glucose uptake and clearance in AD brain with early pathology, which has the potential to facilitate the identification of AD from normal aging.

Chen et al., using a mouse model with tauopathy at 7–8 months old (Fig. 7D), by fitting the initial part of the uptake curves to a simple exponential ($DGE(t) = S_{max}[1-\exp\{-rate \cdot t\}]$), observed a reduction in both the amount (S_{max}) and rate of glucose uptake in parenchyma (Fig. 7E) and in CSF (Fig. 7F). These two studies indicate that imaging CSF and parenchyma with DGE MRI enables the assessment of glymphatic function in AD. In addition to the above studies using D-Glc,[79,80] Tolomeo et al. reported that a reduction of 2-DG uptake in an amyloid plaque AD mouse model was detected by DGE.[83] As mentioned in section 2, some studies have found a competitive inhibition of glycolysis by 2-DG, thus these reported CEST contrast changes in AD should be distinctive from cancers.[84–87]

These early DGE data for the glymphatic system show promise for the possibility to identify early AD pathology, such as a slow-down of D-Glc clearance in the CSF. D-Glc or 2-DG CEST could assess changes in the transport and clearance kinetics of these sugars *in vivo* potentially related to hypometabolism and hypoperfusion in AD. Conventional DCE-MRI has been applied to study the glymphatic system, however the use of GBCAs with intrathecal administration is a concern, in particular in renal compromised and vulnerable populations.[1] Thus, CEST imaging of sugars in the brain may provide unique information for early AD diagnosis.

5.3 Other applications (Placenta, kidneys)

Wu et al. applied DGE MRI to assess mouse placental functioning related to D-glucose utilization.[153] A decrease in glucoCEST contrast was observed for inflamed placenta, possibly due to the decrease in GLUT activity. This could provide a non-invasive approach to study placental disorders, by assessing the glucose uptake of the placental tissue or the fetal-maternal exchange. Another study by Luo et al. reported the feasibility of using DGE MRI to map D-glucose in human placenta using MTR_{asym}.[65] Some issues remain to be addressed for DGE in placenta, such as motion.

Another interesting study is to identify acute renal allograft rejection using glucoCEST.[152] GlucoCEST contrast in MTR_{asym} increased during acute rejection, which could be attributed to the increase in cellular uptake and vascular permeability. This allowed the identification of rejection with high sensitivity and specificity in a rat model.

In summary, several promising applications of glucoCEST have been demonstrated in both preclinical and clinical settings, especially in assessing abnormality of D-glucose-related events. In order to apply glucoCEST for diagnosis and monitoring treatment, challenges, such as a lack of kinetic models for glucose uptake and utilization, motion artifacts and choice of B_0, need to be addressed to bring glucoCEST from initial research studies to wider clinical applications.

6. CHALLENGES AND OPPORTUNITIES

6.1. Physiological Challenges

Like all other contrast agents, there is also a concentration dependency of the CEST effect since the number of solute protons is directly proportional to the effect size.[15] Currently, there is no consensus which D-Glc concentration to use in human experiments. For example, some investigators have used a bolus injection dose of 50mL of 50% w/v dextrose[45,48,53,54], others 100 mL of 20%w/v dextrose.[46,47] Instead of a bolus injection, Kim et al. used 20% dextrose with a clamp infusion where the blood glucose level was raised to a stabilized hyperglycemic level.[50] In this particular study, the approach required up to 12 min to reach the targeted plasma glucose level, which is time consuming compared to the other studies where the infusion durations ranged from 30 s to 4 min.

Depending on the D-Glc concentration by weight and the total infusion amount, some physiological issues may occur. One potential problem is the osmolarity effect induced by high concentration D-Glc solutions, which may affect the observed signal and also cause trauma to the vein and result in thrombophlebitis when infused rapidly.[50,54,173] Seidemo et al.[54] investigated two different D-Glc infusion durations, 1.5 min and 4 min, and concluded that longer infusion duration was preferred because it minimized the side effects while still producing a sufficient change in blood glucose levels. Not only can the thrombophlebitis risk be minimized with longer infusion duration, but the participants in this study also experienced reduced sensory effects when using the longer infusion. Infusion sensory effects that can be felt during D-Glc infusion include a sugary taste in the mouth, warmth, or pulsating feeling at the injection site and in the head and crotch, as well as a need to urinate.

The fasting blood glucose level within the normal range is 70 mg/dL (3.9 mM) to 125 mg/dL (7 mM),[174] which we have used as baseline range for our experiments[45,174] prior to D-Glc infusion. However, some medications such as steroids in tumor patients can cause elevated blood glucose levels, which will prevent the subjects from being eligible. Patients with diabetes mellitus, sickle cell disease, and low blood iron levels are also currently excluded from glucoCEST experiments. The exclusion of these patient groups will hamper the general applicability of glucoCEST and more research is needed to evaluate if some of these patient groups can be included in the future.

6.2. Technical Challenges

Even though several studies have successfully shown a DGE signal change when D-Glc or its analogues have been infused, a major challenge is the rather small effect size in humans. Xu et al. reported a D-Glc based DGE effect of 2–6% in the Gd-enhancing region of a glioma rim at 7T,[45] which reduced to 0.5–1.5% at 3T.[53] The main reason for the difference in effect size with field strength is that the hydroxyl protons exchange rapidly with the surrounding water protons (k_{ex} of approximately 1.5–15 kHz).[51] As discussed in the technical section, when going to lower field, the exchange regime moves from slow-intermediate to intermediate-fast on the MR timescale, leading to increased coalescence with the water resonance[27] and a reduction in detectability of the hydroxyl CEST effect (Fig. 4).[50] While higher field strengths are preferred due to the increased separation between the

hydroxyl protons and water protons, ultra-high human field human scanners (≥7T) come with other problems, such as increased inhomogeneity in the B_0 field and the RF transmit field (B_{1+}). Even though B_0 and B_1^+ shimming methods have been developed to mitigate these effects,[175–177] in order to have impact, the methods ultimately need to be available at clinical field strengths (i.e. 3T and lower).

Partial volume effects (PVE) are common in MR images due to the limited resolution used to achieve adequate SNR. In DGE the voxel volume usually ranges to 14 to 48 mm^3 depending on pulse sequence, field strength and target volume which leads to different amounts of PVE. A major problem with PVE in DGE, that is not related to the usual mixing of different tissues, is that the glucose infusion also leads to some ventricular swelling. This swelling, that is in the order of 1–2%,[54] can cause additional CSF to be mixed with tissue during the acquisition, thus creating erroneous hyperintensities due to the large D-Glc concentration in CSF or hyper/hypointensities due to CSF pulsation.

Image hyper- and hypointensities can also occur due to patient movement that causes local B_0 changes in tissue and concomitant shifts of the resonance frequency. Zaiss et al. demonstrated that, when using difference images obtained at a single frequency, motion and B_0 shifts can signal changes on the order of ±1%,[178] the same effect size as reported from DGE studies at 3T (Figures 8A–F). The hyperintensities, caused by a field shift, can therefore be mistaken as real CEST effects. These artifactual CEST effects have been dubbed as “pseudo CEST effects”. Performing standard motion correction algorithms will reduce these pseudo CEST effects,[52] however, when applying these, there is a risk that true DGE signal can be mistaken for motion and altered erroneously. This warrants for more advanced motion correction post-processing methods or the use of volumetric navigators before the saturation period in the acquisition.[179] Despite the problems with motion, DGE remains a promising technique, as illustrated in Figures 8G–R. These results from Xu et al.[45] obtained at a 7T scanner in a brain tumor patient (Figure 8G–J) clearly show that the rim around the necrotic region in a tumor enhances rapidly (Figure 8H), providing contrast similar to DCE, whereas the tumor center and surrounding tissue enhance more slowly (Figure 8I,J), providing information not available in DCE. At 3T the issue with motion becomes more imperative due to the smaller CEST effect. However Herz et al[52] and Xu et al.[53] demonstrated that, despite these challenges (Figure 8K–R), a DGE signal increase was still observable at 3T in patients with brain tumors. Additionally, in some cases, the increased DGE signal in the tumor corresponded to the Gd enhanced location, particularly in the later stages of the DGE imaging (Figure 8N,R).

Another challenging issue before DGE MRI can be used clinically is the acquisition time. Papers have reported scan times ranging from 15 to 60 min with temporal resolutions ranging from 5.3 to 42 seconds.[45–48,50,53,54,66] Not only are longer scan times more prone to motion artefacts, but they can also make the patient feel more uncomfortable and anxious. Faster acquisition techniques such as simultaneous multi-slice imaging[180,181] and compressed sensing[182,183] that reduce the scan duration are available. However, reaching typical MRI scans of 5 minutes is not possible when a long baseline is needed (previous literature has reported baseline times of 3 minutes) for the purpose of SNR and when

the infusion duration is recommended to be 4 minutes for the patient to be comfortable physiologically due to the amounts of sugar needed.

6.3. Opportunities

Based on the above considerations, increased SNR/CNR is the most important opportunity to be pursued for the field to be moved forward. This is in principle possible through the design of new pulse sequences with increased sensitivity, such as for instance pulsed approaches (e.g. the onVDMP method) in which a larger fraction (broader chemical shift range) of fast-exchanging protons is labelled rapidly and repeatedly (i.e. after exchange). In addition, recent papers indicate that reduced amounts of GBCAs can be used with properly trained artificial intelligence approaches[184,185], which one would think should also be possible for DGE.

The simplest approach for increasing effect size is increasing the amount of sugar infused, but that is very limited. More promising, the use of alternative sugars with different physiological properties provides promising opportunities. Currently, only D-Glc has been used in human glucoCEST experiments. However, there is a large interest in other sugars such as 3-OMG and D-GlcN that accumulate in the tumor. It has for instance been shown in studies by Rivlin et al. 2014 and Sehgal et al. 2019,[57,59] that, when used at the same concentration, 3-OMG induces a CEST contrast effect that is larger than that of D-Glc with up to twice the contrast enhancement in tumor tissue.[59] Although no toxicology studies of 3-OMG have been reported, mice or rats given various doses of 3-OMG have not shown any physiological or behavioral changes.[186] Since 3-OMG has been used to study intestinal permeability in humans[104,105] it is probable that 3-OMG can be translated into the clinic as a glucoCEST agent if suitable concentrations can be used. Very recently, the first human studies of D-GlcN demonstrated the possibility to highlight breast tumors.[101]

7. CONCLUSIONS

CEST imaging of D-Glc and other sugars in principle provides a minimally-invasive way to detect their related delivery, transport and metabolism *in vivo*, without the need of radioactive or metallic labeling. Recent compartmental studies based on glucose-related physiology and pathology help to elucidate the potential contributions to the glucoCEST signal, but the availability of a single uptake curve complicates interpretation. Despite this, several animal studies are showing the possibility to detect alterations of sugar transport/clearance and/or uptake in cancers, Alzheimer's disease, placenta and during kidney allograft rejection. Also, several small sugars such as 3-OMG and D-GlcN may be available for human studies soon. Remaining challenges are many but expected to be addressable when methodological advances become available. We are therefore cautiously optimistic that such advances in MRI detection and data analysis as well as availability of more sugar analogues will allow this young field to steadily move forward in the coming years.

ACKNOWLEDGMENTS

Authors are grateful to receive funding support from the Research Grants Council: 11102218, PDFS2122-1S01, C1134-20G; City University of Hong Kong: 7005433, 7005626, 9667198, 9609307 and 9610560; National Natural Science Foundation of China: 81871409; Hong Kong Center for Cerebro-cardiovascular Health Engineering

(COCHE); Tung Biomedical Sciences Centre; Swedish Research Council grant numbers 2019-03637; Swedish Cancer Society grant numbers CAN 2018/550 and 21 1652 Pj; Swedish Brain Foundation grant number FO2021-0328; and National Institutes of Health grant numbers RO1 EB019934 and R00 EB026312. We would like to thank Dr. J. Huang and Ms Z. Chen for assisting with table 1.

ABBREVIATIONS

(c)	Intracellular
2-DG	2-Deoxy-D-glucose
3-OMG	3-orthomethyl-D-glucose
AD	Alzheimer's disease
AIF	Arterial input function
AUC	Area under the curve
BBB	Blood brain barrier
BOLD	blood oxygen level-dependent
CESL	Chemical exchange sensitive spin-lock
CEST	Chemical exchange saturation transfer
CPMG	Carr-Purcell-Meiboom-Gill
CSF	Cerebral spinal fluid
CT	Computed tomography
CW	Continuous wave
DCE	Dynamic contrast enhanced
DGE	Dynamic glucose enhanced
D-Glc	D-glucose
D-GlcN	D-glucosamine (2-amino-2-deoxy-D-glucose)
D-Xyl	D-Xylose
EES, (e)	Extravascular and extracellular space
FDG	Fluorodeoxyglucose
GBCA	Gadolinium based contrast agent
Gd	Gadolinium
GdDTPA	Gadolinium diethylenetriamine penta-acetic acid
GlcNAc	N-acetyl-D-glucosamine

glucoCESL	glucose CESL
glucoCEST	glucose CEST
GLUT	Glucose transporter
ISF	Interstitial fluid
i.v.	Intravenous
k_{ex}	Exchange rate
K^{trans}	Volume transfer constant
L-Glc	L-glucose
Mls	Maltose
Mlt	Maltitol
mTOR	Mechanistic target of rapamycin kinase
MTR_{asym}	Magnetization transfer ratio with asymmetric analysis
onVDMP	on-resonance variable delay multi-pulse
PET	Positron emission tomography
p.o.	per os
PSMA	Prostate specific membrane antigen
PVE	Partial volume effect
RF	Radiofrequency
SAR	Specific absorption rate
S_{base}	Average baseline signal
Slc	Sucralose
TCA	Tricarboxylic acid
TSL	Time of Spin-lock (duration)
(v)	Vascular
WT	Wild-type

REFERENCES

1. Lohrke J, Frenzel T, Endrikat J, et al. 25 years of contrast-enhanced MRI: developments, current challenges and future perspectives. Adv Ther. 2016;33(1):1–28. [PubMed: 26809251]
2. Robert P, Fingerhut S, Factor C, et al. One-year retention of gadolinium in the brain: comparison of gadodiamide and gadoterate meglumine in a rodent model. Radiology. 2018;288(2):424–433. [PubMed: 29786486]

3. Marckmann P, Skov L, Rossen K, et al. Nephrogenic systemic fibrosis: suspected causative role of gadodiamide used for contrast-enhanced magnetic resonance imaging. J Am Soc Nephrol. 2006;17(9):2359–2362. [PubMed: 16885403]
4. Thomsen HS, Morcos SK, Almén T, et al. Nephrogenic systemic fibrosis and gadolinium-based contrast media: updated ESUR Contrast Medium Safety Committee guidelines. Eur Radiol. 2013;23(2):307–318. [PubMed: 22865271]
5. Krzeslak A, Wojcik-Krowiranda K, Forma E, et al. Expression of GLUT1 and GLUT3 glucose transporters in endometrial and breast cancers. Pathol Oncol Res. 2012;18(3):721–728. [PubMed: 22270867]
6. Kanda T, Ishii K, Kawaguchi H, Kitajima K, Takenaka D. High signal intensity in the dentate nucleus and globus pallidus on unenhanced T1-weighted MR images: relationship with increasing cumulative dose of a gadolinium-based contrast material. Radiology. 2014;270(3):834–841. [PubMed: 24475844]
7. Errante Y, Cirimele V, Mallio CA, Di Lazzaro V, Zobel BB, Quattrocchi CC. Progressive increase of T1 signal intensity of the dentate nucleus on unenhanced magnetic resonance images is associated with cumulative doses of intravenously administered gadodiamide in patients with normal renal function, suggesting dechelation. Invest Radiol. 2014;49(10):685–690. [PubMed: 24872007]
8. McDonald RJ, McDonald JS, Kallmes DF, et al. Intracranial gadolinium deposition after contrast-enhanced MR imaging. Radiology. 2015;275(3):772–782. [PubMed: 25742194]
9. Robert P, Lehericy S, Grand S, et al. T1-weighted hypersignal in the deep cerebellar nuclei after repeated administrations of gadolinium-based contrast agents in healthy rats: difference between linear and macrocyclic agents. Invest Radiol. 2015;50(8):473. [PubMed: 26107651]
10. Lord ML, Chettle DR, Gräfe JL, Noseworthy MD, McNeill FE. Observed deposition of gadolinium in bone using a new noninvasive in vivo biomedical device: results of a small pilot feasibility study. Radiology. 2018;287(1):96–103. [PubMed: 29237148]
11. Wolff SD, Balaban RS. Magnetization transfer contrast (MTC) and tissue water proton relaxation in vivo. Magn Reson Med. 1989;10(1):135–144. [PubMed: 2547135]
12. Ward K, Aletras A, Balaban RS. A new class of contrast agents for MRI based on proton chemical exchange dependent saturation transfer (CEST). J Magn Reson. 2000;143(1):79–87. [PubMed: 10698648]
13. Gore J, Brown M, Mizumoto C, Armitage I. Influence of glycogen on water proton relaxation times. Magn Reson Med. 1986;3(3):463–466. [PubMed: 3724426]
14. Hills B, Takacs S, Belton P. The effects of proteins on the proton NMR transverse relaxation times of water: I. Native bovine serum albumin. Mol Phys. 1989;67(4):903–918.
15. Van Zijl PC, Yadav NN. Chemical exchange saturation transfer (CEST): what is in a name and what isn't? Magn Reson Med. 2011;65(4):927–948. [PubMed: 21337419]
16. Jin T, Autio J, Obata T, Kim SG. Spin-locking versus chemical exchange saturation transfer MRI for investigating chemical exchange process between water and labile metabolite protons. Magn Reson Med. 2011;65(5):1448–60. [PubMed: 21500270]
17. Yadav NN, Xu J, Bar-Shir A, et al. Natural D-glucose as a biodegradable MRI relaxation agent. Magn Reson Med. 2014;72(3):823–8. [PubMed: 24975029]
18. Goldenberg JM, Pagel MD, Cárdenas-Rodríguez J. Characterization of D-maltose as a T2-exchange contrast agent for dynamic contrast-enhanced MRI. Magn Reson Med. 2018;80(3):1158–1164. [PubMed: 29369407]
19. Huang J, Lai JHC, Han X, et al. Sensitivity schemes for dynamic glucose-enhanced magnetic resonance imaging to detect glucose uptake and clearance in mouse brain at 3 T. NMR Biomed. 2021:e4640. [PubMed: 34750891]
20. Aime S, Calabi L, Biondi L, et al. Iopamidol: Exploring the potential use of a well-established x-ray contrast agent for MRI. Magn Reson Med. 2005;53(4):830–834. [PubMed: 15799043]
21. Longo DL, Busato A, Lanzardo S, Antico F, Aime S. Imaging the pH evolution of an acute kidney injury model by means of iopamidol, a MRI-CEST pH-responsive contrast agent. Magn Reson Med. 2013;70(3):859–864. [PubMed: 23059893]

22. Sun PZ, Longo DL, Hu W, Xiao G, Wu R. Quantification of iopamidol multi-site chemical exchange properties for ratiometric chemical exchange saturation transfer (CEST) imaging of pH. Phys Med Biol. 2014;59(16):4493. [PubMed: 25054859]

23. Lindeman LR, Randtke EA, High RA, Jones KM, Howison CM, Pagel MD. A comparison of exogenous and endogenous CEST MRI methods for evaluating in vivo p H. Magn Reson Med. 2018;79(5):2766–2772. [PubMed: 29024066]

24. Chen LQ, Howison CM, Jeffery JJ, Robey IF, Kuo PH, Pagel MD. Evaluations of extracellular pH within in vivo tumors using acidoCEST MRI. Magn Reson Med. 2014;72(5):1408–1417. [PubMed: 24281951]

25. Melkus G, Grabau M, Karampinos DC, Majumdar S. Ex vivo porcine model to measure pH dependence of chemical exchange saturation transfer effect of glycosaminoglycan in the intervertebral disc. Magn Reson Med. 2014;71(5):1743–1749. [PubMed: 23818244]

26. Yang X, Song X, Li Y, et al. Salicylic acid and analogues as diaCEST MRI contrast agents with highly shifted exchangeable proton frequencies. Angew Chem. 2013;125(31):8274–8277.

27. Banerjee SR, Song X, Yang X, et al. Salicylic acid-based polymeric contrast agents for molecular magnetic resonance imaging of prostate cancer. Chemistry. 2018;24(28):7235. [PubMed: 29508450]

28. Li Y, Chen H, Xu J, et al. CEST theranostics: label-free MR imaging of anticancer drugs. Oncotarget. 2016;7(6):6369. [PubMed: 26837220]

29. Rivlin M, Navon G. Molecular imaging of tumors by chemical exchange saturation transfer MRI of glucose analogs. Quant Imaging Med Surg. 2019;9(10):1731. [PubMed: 31728315]

30. Paech D, Radbruch A. Dynamic Glucose-Enhanced MR Imaging. Magn Reson Imaging Clin N Am. 2021;29(1):77–81. [PubMed: 33237017]

31. Liu G, Banerjee SR, Yang X, et al. A dextran-based probe for the targeted magnetic resonance imaging of tumours expressing prostate-specific membrane antigen. Nat Biomed Eng. 2017;1(12):977–982. [PubMed: 29456877]

32. Li Y, Qiao Y, Chen H, et al. Characterization of tumor vascular permeability using natural dextrans and CEST MRI. Magn Reson Med. 2018;79(2):1001–1009. [PubMed: 29193288]

33. Han Z, Zhang S, Fujiwara K, et al. Extradomain-B fibronectin-targeted dextran-based chemical exchange saturation transfer magnetic resonance imaging probe for detecting pancreatic cancer. Bioconj Chem. 2019;30(5):1425–1433.

34. Chen H, Liu D, Li Y, et al. CEST MRI monitoring of tumor response to vascular disrupting therapy using high molecular weight dextrans. Magn Reson Med. 2019;82(4):1471–1479. [PubMed: 31106918]

35. Consolino L, Irrera P, Romdhane F, Anemone A, Longo DL. Investigating plasma volume expanders as novel macromolecular MRI-CEST contrast agents for tumor contrast-enhanced imaging. Magn Reson Med. 2021;86(2):995–1007. [PubMed: 33764575]

36. Van Zijl PC, Jones CK, Ren J, Malloy CR, Sherry AD. MRI detection of glycogen in vivo by using chemical exchange saturation transfer imaging (glycoCEST). Proc Natl Acad Sci U S A. 2007;104(11):4359–4364. [PubMed: 17360529]

37. Zhou Y, van Zijl PC, Xu X, et al. Magnetic resonance imaging of glycogen using its magnetic coupling with water. Proc Natl Acad Sci U S A. 2020;117(6):3144–3149. [PubMed: 32001509]

38. Arsov T, Mullen SA, Damiano JA, et al. Early onset absence epilepsy: 1 in 10 cases is caused by GLUT1 deficiency. Epilepsia. Dec 2012;53(12):e204–7. doi:10.1111/epi.12007 [PubMed: 23106342]

39. Kapogiannis D, Mattson MP. Disrupted energy metabolism and neuronal circuit dysfunction in cognitive impairment and Alzheimer's disease. Lancet Neurol. Feb 2011;10(2):187–98. [PubMed: 21147038]

40. Kim M, Eleftheriou A, Ravotto L, et al. What do we know about dynamic glucose-enhanced (DGE) MRI and how close is it to the clinics? Horizon 2020 GLINT consortium report. MAGMA. 2022;35:87–104. [PubMed: 35032288]

41. Chan KW, McMahon MT, Kato Y, et al. Natural D-glucose as a biodegradable MRI contrast agent for detecting cancer. Magn Reson Med. 2012;68(6):1764–73. [PubMed: 23074027]

42. Walker-Samuel S, Ramasawmy R, Torrealdea F, et al. In vivo imaging of glucose uptake and metabolism in tumors. Nat Med. 2013;19(8):1067–1072. [PubMed: 23832090]
43. Jin T, Mehrens H, Hendrich KS, Kim S-G. Mapping brain glucose uptake with chemical exchange-sensitive spin-lock magnetic resonance imaging. J Cereb Blood Flow Metab. 2014;34(8):1402–1410. [PubMed: 24865996]
44. Xu X, Chan KW, Knutsson L, et al. Dynamic glucose enhanced (DGE) MRI for combined imaging of blood-brain barrier break down and increased blood volume in brain cancer. Magn Reson Med. 2015;74(6):1556–63. [PubMed: 26404120]
45. Xu X, Yadav NN, Knutsson L, et al. Dynamic glucose-enhanced (DGE) MRI: translation to human scanning and first results in glioma patients. Tomography. 2015;1(2):105–114. [PubMed: 26779568]
46. Paech D, Schuenke P, Koehler C, et al. T1rho-weighted Dynamic Glucose-enhanced MR Imaging in the Human Brain. Case Reports. Radiology. 2017;285(3):914–922. [PubMed: 28628422]
47. Schuenke P, Paech D, Koehler C, et al. Fast and Quantitative T1rho-weighted Dynamic Glucose Enhanced MRI. Sci Rep. 2017;7:42093. [PubMed: 28169369]
48. Knutsson L, Seidemo A, Scherman AR, et al. Arterial input functions and tissue response curves in dynamic glucose-enhanced (DGE) Imaging: Comparison between glucoCEST and blood glucose sampling in humans. Tomography. 2018;4(4):164–171. [PubMed: 30588502]
49. Jin T, Iordanova B, Hitchens TK, et al. Chemical exchange–sensitive spin-lock (CESL) MRI of glucose and analogs in brain tumors. Magn Reson Med. 2018;80(2):488–495. [PubMed: 29569739]
50. Kim M, Torrealdea F, Adeleke S, et al. Challenges in glucoCEST MR body imaging at 3 Tesla. Quant Imaging Med Surg. 2019;9(10):1628–1640. [PubMed: 31728307]
51. Zaiss M, Anemone A, Goerke S, et al. Quantification of hydroxyl exchange of D-Glucose at physiological conditions for optimization of glucoCEST MRI at 3, 7 and 9.4 Tesla. NMR Biomed. 2019;32(9):e4113. [PubMed: 31313865]
52. Herz K, Lindig T, Deshmane A, et al. T1rho-based dynamic glucose-enhanced (DGErho) MRI at 3 T: method development and early clinical experience in the human brain. Magn Reson Med. 2019;82(5):1832–1847. [PubMed: 31231853]
53. Xu X, Sehgal AA, Yadav NN, et al. d-glucose weighted chemical exchange saturation transfer (glucoCEST)-based dynamic glucose enhanced (DGE) MRI at 3T: early experience in healthy volunteers and brain tumor patients. Magn Reson Med. 2020;84(1):247–262. [PubMed: 31872916]
54. Seidemo A, Lehmann PM, Rydhög A, et al. Towards robust glucose chemical exchange saturation transfer imaging in humans at 3 T: Arterial input function measurements and the effects of infusion time. NMR Biomed. 2021:e4624. [PubMed: 34585813]
55. Nasrallah FA, Pagès G, Kuchel PW, Golay X, Chuang K-H. Imaging brain deoxyglucose uptake and metabolism by glucoCEST MRI. J Cereb Blood Flow Metab. 2013;33(8):1270–1278. [PubMed: 23673434]
56. Jin T, Mehrens H, Wang P, Kim S-G. Glucose metabolism-weighted imaging with chemical exchange-sensitive MRI of 2-deoxyglucose (2-DG) in brain: Sensitivity and biological sources. NeuroImage. 2016/12/01/ 2016;143:82–90. [PubMed: 27570111]
57. Rivlin M, Tsarfaty I, Navon G. Functional molecular imaging of tumors by chemical exchange saturation transfer MRI of 3-O-Methyl-D-glucose. Magn Reson Med. 2014;72(5):1375–80. [PubMed: 25236979]
58. Jin T, Mehrens H, Wang P, Kim S-G. Chemical exchange-sensitive spin-lock MRI of glucose analog 3-O-methyl-d-glucose in normal and ischemic brain. J Cereb Blood Flow Metab. 2018;38(5):869–880. [PubMed: 28485194]
59. Sehgal AA, Li Y, Lal B, et al. CEST MRI of 3-O-methyl-D-glucose uptake and accumulation in brain tumors. Magn Reson Med. 2019;81(3):1993–2000. doi:10.1002/mrm.27489 [PubMed: 30206994]
60. Anemone A, Capozza M, Arena F, et al. In vitro and in vivo comparison of MRI chemical exchange saturation transfer (CEST) properties between native glucose and 3-O-Methyl-D-glucose in a murine tumor model. NMR Biomed. 2021:e4602. [PubMed: 34423470]

61. Rivlin M, Navon G. Glucosamine and N-acetyl glucosamine as new CEST MRI agents for molecular imaging of tumors. Sci Rep. 2016;6(1):1–7. [PubMed: 28442746]
62. Rivlin M, Navon G. Molecular imaging of cancer by glucosamine chemical exchange saturation transfer MRI: A preclinical study. NMR Biomed. 2021;34(2):e4431. [PubMed: 33103831]
63. Wang J, Weygand J, Hwang K-P, et al. Magnetic resonance imaging of glucose uptake and metabolism in patients with head and neck cancer. Sci Rep. 2016;6(1):1–7. [PubMed: 28442746]
64. Schuenke P, Koehler C, Korzowski A, et al. Adiabatically prepared spin-lock approach for T1rho-based dynamic glucose enhanced MRI at ultrahigh fields. Magn Reson Med. 2017;78(1):215–225. [PubMed: 27521026]
65. Luo J, Turk EA, Gagoski B, et al. Preliminary evaluation of dynamic glucose enhanced MRI of the human placenta during glucose tolerance test. Quant Imaging Med Surg. 2019;9(10):1619. [PubMed: 31728306]
66. Boyd PS, Breitling J, Zimmermann F, et al. Dynamic glucose-enhanced (DGE) MRI in the human brain at 7 T with reduced motion-induced artifacts based on quantitative R1rho mapping. Magn Reson Med. 2020;84(1):182–191. [PubMed: 31788870]
67. Sokoloff L, Reivich M, Kennedy C, et al. The [14C]deoxyglucose method for the measurement of local cerebral glucose utilization: theory, procedure, and normal values in the conscious and anesthetized albino rat. J Neurochem. 1977;28(5):897–916. [PubMed: 864466]
68. Van Zijl PC, Davis D, Eleff SM, Moonen CT, Parker RJ, Strong JM. Determination of cerebral glucose transport and metabolic kinetics by dynamic MR spectroscopy. Am J Physiol. 1997;273(6):E1216–27. [PubMed: 9435539]
69. de Graaf RA, Mason GF, Patel AB, Behar KL, Rothman DL. In vivo 1H-[13C]-NMR spectroscopy of cerebral metabolism. NMR Biomed. 2003;16(6–7):339–57. [PubMed: 14679499]
70. Lanz B, Gruetter R, Duarte JM. Metabolic Flux and Compartmentation Analysis in the Brain In vivo. Front Endocrinol. 2013;4:156.
71. Hui S, Ghergurovich JM, Morscher RJ, et al. Glucose feeds the TCA cycle via circulating lactate. Nature. 2017;551(7678):115–118. [PubMed: 29045397]
72. Newsholme P, Procopio J, Lima MMR, Pithon-Curi TC, Curi R. Glutamine and glutamate—their central role in cell metabolism and function. Cell Biochem Funct. 2003;21(1):1–9. [PubMed: 12579515]
73. Liepinsh E, Otting G. Proton exchange rates from amino acid side chains--implications for image contrast. Magn Reson Med. 1996;35(1):30–42. [PubMed: 8771020]
74. Englander SW, Kallenbach NR. Hydrogen exchange and structural dynamics of proteins and nucleic acids. Q Rev Biophys. 1983;16(4):521–655. [PubMed: 6204354]
75. van Zijl PCM, Lam WW, Xu J, Knutsson L, Stanisz GJ. Magnetization Transfer Contrast and Chemical Exchange Saturation Transfer MRI. Features and analysis of the field-dependent saturation spectrum. NeuroImage. 2018;168:222–241. [PubMed: 28435103]
76. Zhou J, van Zijl PC. Chemical exchange saturation transfer imaging and spectroscopy. Prog Nucl Magn Reson Spectrosc. 2006;48(2/3):109–136.
77. Bingley PJ, Colman P, Eisenbarth GS, et al. Standardization of IVGTT to predict IDDM. Diabetes Care. 1992;15(10):1313–1316. [PubMed: 1425095]
78. Ikkos D, Luft R. On the intravenous glucose tolerance test. Eur J Endocrinol. 1957;25(3):312–334.
79. Huang J, van Zijl PCM, Han X, et al. Altered d-glucose in brain parenchyma and cerebrospinal fluid of early Alzheimer's disease detected by dynamic glucose-enhanced MRI. Sci Adv. 2020;6(20):eaba3884. [PubMed: 32426510]
80. Chen L, Wei Z, Chan KW, et al. D-Glucose uptake and clearance in the tauopathy Alzheimer's disease mouse brain detected by on-resonance variable delay multiple pulse MRI. J Cereb Blood Flow. 2021;41(5):1013–1025.
81. Zu Z, Spear J, Li H, Xu J, Gore JC. Measurement of regional cerebral glucose uptake by magnetic resonance spin-lock imaging. Magn Reson Imaging. 2014;32(9):1078–84. [PubMed: 24960367]
82. Rivlin M, Horev J, Tsarfaty I, Navon G. Molecular imaging of tumors and metastases using chemical exchange saturation transfer (CEST) MRI. Sci Rep. 2013;3:3045. [PubMed: 24157711]

83. Tolomeo D, Micotti E, Serra SC, Chappell M, Snellman A, Forloni G. Chemical exchange saturation transfer MRI shows low cerebral 2-deoxy-D-glucose uptake in a model of Alzheimer's Disease. Sci Rep. 2018;8(1):1–10. [PubMed: 29311619]
84. Kurtoglu M, Maher JC, Lampidis TJ. Differential toxic mechanisms of 2-deoxy-D-glucose versus 2-fluorodeoxy-D-glucose in hypoxic and normoxic tumor cells. Antioxid Redox Signal. 2007;9(9):1383–90. [PubMed: 17627467]
85. Zhao J, Ma Y, Zhang Y, et al. Low-dose 2-deoxyglucose and metformin synergically inhibit proliferation of human polycystic kidney cells by modulating glucose metabolism. Cell Death Discov. 2019;5:76. [PubMed: 30886744]
86. Pantic B, Ives D, Mennuni M, et al. 2-Deoxy-D-glucose couples mitochondrial DNA replication with mitochondrial fitness and promotes the selection of wild-type over mutant mitochondrial DNA. Nat Commun. 2021;12(1):6997. [PubMed: 34873176]
87. Vijayaraghavan R, Kumar D, Dube S, et al. Acute toxicity and cardio-respiratory effects of 2-deoxy-D-glucose: a promising radio sensitiser. Biomed Environ Sci. 2006;19(2):96–103. [PubMed: 16827179]
88. Uldry M, Ibberson M, Hosokawa M, Thorens B. GLUT2 is a high affinity glucosamine transporter. FEBS Lett. 2002;524(1–3):199–203. [PubMed: 12135767]
89. Anderson J, Nicolosi R, Borzelleca J. Glucosamine effects in humans: a review of effects on glucose metabolism, side effects, safety considerations and efficacy. Food Chem Toxicol. 2005;43(2):187–201. [PubMed: 15621331]
90. Little PJ, Drennon KD, Tannock LR. Glucosamine inhibits the synthesis of glycosaminoglycan chains on vascular smooth muscle cell proteoglycans by depletion of ATP. Arch Physiol Biochem. 2008;114(2):120–126. [PubMed: 18484279]
91. Salazar J, Bello L, Chávez M, Añez R, Rojas J, Bermúdez V. Glucosamine for osteoarthritis: biological effects, clinical efficacy, and safety on glucose metabolism. Arthritis. 2014;2014
92. Monauni T, Zenti MG, Cretti A, et al. Effects of glucosamine infusion on insulin secretion and insulin action in humans. Diabetes. 2000;49(6):926–935. [PubMed: 10866044]
93. Pouwels M-JJ, Jacobs JR, Span PN, Lutterman JA, Smits P, Tack CJ. Short-term glucosamine infusion does not affect insulin sensitivity in humans. J Clin Endocrinol Metab. 2001;86(5):2099–2103. [PubMed: 11344213]
94. Vangsness CT Jr, Spiker W, Erickson J. A review of evidence-based medicine for glucosamine and chondroitin sulfate use in knee osteoarthritis. Arthrosc - J Arthrosc Relat Surg. 2009;25(1):86–94.
95. Salvatore S, Heuschkel R, Tomlin S, et al. A pilot study of N-acetyl glucosamine, a nutritional substrate for glycosaminoglycan synthesis, in paediatric chronic inflammatory bowel disease. Aliment Pharmacol Ther. 2000;14(12):1567–1579. [PubMed: 11121904]
96. Persiani S, Roda E, Rovati L, Locatelli M, Giacovelli G, Roda A. Glucosamine oral bioavailability and plasma pharmacokinetics after increasing doses of crystalline glucosamine sulfate in man. Osteoarthr Cartil. 2005;13(12):1041–1049.
97. Tannis AJ, Barban J, Conquer JA. Effect of glucosamine supplementation on fasting and non-fasting plasma glucose and serum insulin concentrations in healthy individuals. Osteoarthr Cartil. 2004;12(6):506–511.
98. Simon R, Marks V, Leeds A, Anderson J. A comprehensive review of oral glucosamine use and effects on glucose metabolism in normal and diabetic individuals. Diabetes Metab Res Rev. 2011;27(1):14–27. [PubMed: 21218504]
99. Popov N. Effects of D-galactosamine and D-glucosamine on retention performance of a brightness discrimination task in rats. Biomed Biochim Acta. 1985;44(4):611–622. [PubMed: 4026816]
100. Sy M, Brandt AU, Lee S-U, et al. N-acetylglucosamine drives myelination by triggering oligodendrocyte precursor cell differentiation. Journal of Biological Chemistry. 2020;295(51):17413–17424. [PubMed: 33453988]
101. Rivlin M, Anaby D, Nissan N, et al. Molecular imaging of breast cancer by chemical exchange saturation transfer (CEST) MRI of glucosamine: first human experience. Proc Int Soc Magn Reson Med. 2022;31:2799.
102. Rivlin M, Navon G. CEST MRI of 3-O-methyl-D-glucose on different breast cancer models. Magn Reson Med. 2018;79(2):1061–1069. [PubMed: 28497566]

103. Rivlin M, Navon G. 3-O-Methyl-D-glucose mutarotation and proton exchange rates assessed by (13)C, (1)H NMR and by chemical exchange saturation transfer and spin lock measurements. J Biomol NMR. 2018;72(1–2):93–103. [PubMed: 30203383]
104. Sigalet DL, Martin GR, Meddings JB. 3–0 methylglucose uptake as a marker of nutrient absorption and bowel length in pediatric patients. JPEN J Parenter Enteral Nutr. 2004;28(3):158–62. [PubMed: 15141408]
105. Jenkins AP, Menzies IS, Nukajam WS, Creamer B. The effect of ingested lactulose on absorption of L-rhamnose, D-xylose, and 3-O-methyl-D-glucose in subjects with ileostomies. Scand J Gastroenterol. 1994;29(9):820–5. [PubMed: 7824862]
106. Minn AH, Couto FM, Shalev A. Metabolism-independent sugar effects on gene transcription: the role of 3-O-methylglucose. Biochemistry. 2006;45(37):11047–51. [PubMed: 16964965]
107. Smeets PA, Vidarsdottir S, de Graaf C, et al. Oral glucose intake inhibits hypothalamic neuronal activity more effectively than glucose infusion. Am J Physiol - Endocrinol Metab. 2007;293(3):E754–8. [PubMed: 17566114]
108. Wang J, Fukuda M, Chung JJ, Wang P, Jin T. Chemical exchange sensitive MRI of glucose uptake using xylose as a contrast agent. Magn Reson Med. 2021;85(4):1953–1961. [PubMed: 33107108]
109. Fordtran JS, Clodi PH, Soergel KH, Ingelfinger FJ. Sugar absorption tests, with special reference to 3–0-methyl-d-glucose and d-xylose. Ann Intern Med. 1962;57(6):883–891. [PubMed: 13958713]
110. LeFevre PG, Peters AA. Evidence of mediated transfer of monosaccharides from blood to brain in rodents. J Neurochem. 1966;13(1):35–46. [PubMed: 5931178]
111. Carlson S, Craig RM. D-Xylose hydrogen breath tests compared to absorption kinetics in human patients with and without malabsorption. Dig Dis Sci. 1995;40(10):2259–2267. [PubMed: 7587799]
112. Worwag EM, Craig RM, Jansyn EM, Kirby D, Hubler GL, Atkinson AJ Jr. D-Xylose absorption and disposition in patients with moderately impaired renal function. Clin Pharm Therap. 1987;41(3):351–357.
113. Goodwin NC, Mabon R, Harrison BA, et al. Novel L-xylose derivatives as selective sodium-dependent glucose cotransporter 2 (SGLT2) inhibitors for the treatment of type 2 diabetes. J Med Chem. 2009;52(20):6201–6204. [PubMed: 19785435]
114. Wu T, Bound MJ, Zhao BR, et al. Effects of a D-xylose preload with or without sitagliptin on gastric emptying, glucagon-like peptide-1, and postprandial glycemia in type 2 diabetes. Diabetes Care. 2013;36(7):1913–1918. [PubMed: 23359361]
115. Schroder H, Leichtweiss HP, Madee W. The transport of D-glucose, L-glucose and D-mannose across the isolated guinea pig placenta. Pflugers Arch. 1975;356(3):267–75. [PubMed: 1171444]
116. Lucchesi KJ, Gosselin RE. Mechanism of L-glucose, raffinose, and inulin transport across intact blood-brain barriers. Am J Physiol. 1990;258(3 Pt 2):H695–705. [PubMed: 2316684]
117. Ono K, Takigawa S, Yamada K. L-Glucose: Another Path to Cancer Cells. Review. Cancers (Basel) 2020;12(4).
118. Anastasiou IA, Eleftheriadou I, Tentolouris A, Mourouzis I, Pantos C, Tentolouris N. The Use of L-Glucose in Cancer Diagnosis: Results from In Vitro and In Vivo Studies. Review. Curr Med Chem 2021;28(30):6110–6122. [PubMed: 33719949]
119. Buhler I, Walter R, Reinhart WH. Influence of D- and L-glucose on erythrocytes and blood viscosity. Eur J Clin Invest. 2001;31(1):79–85. [PubMed: 11168442]
120. Raymer GS, Hartman DE, Rowe WA, Werkman RF, Koch KL. An open-label trial of L-glucose as a colon-cleansing agent before colonoscopy. Gastrointest Endosc. 2003;58(1):30–5. [PubMed: 12838217]
121. Bagga P, Haris M, D'Aquilla K, et al. Non-caloric sweetener provides magnetic resonance imaging contrast for cancer detection. J Transl Med. 2017;15(1):1–9. [PubMed: 28049494]
122. Bagga P, Wilson N, Rich L, et al. Sugar alcohol provides imaging contrast in cancer detection. Sci Rep. 2019;9(1):1–9. [PubMed: 30626917]
123. Grice HC, Goldsmith LA. Sucralose--an overview of the toxicity data. Food Chem Toxicol. 2000;38 Suppl 2:S1–6.

124. Schiffman SS, Rother KI. Sucralose, a synthetic organochlorine sweetener: overview of biological issues. J Toxicol Environ Health B Crit Rev. 2013;16(7):399–451. [PubMed: 24219506]

125. Suez J, Korem T, Zeevi D, et al. Artificial sweeteners induce glucose intolerance by altering the gut microbiota. Nature. 2014;514(7521):181–6. [PubMed: 25231862]

126. Greenhill C. Metabolic effects of sucralose. Nat Rev Endocrinol. 2020;16(5):256–257.

127. Ruiz-Ojeda FJ, Plaza-Diaz J, Saez-Lara MJ, Gil A. Effects of Sweeteners on the Gut Microbiota: A Review of Experimental Studies and Clinical Trials. Adv Nutr. Jan 1 2019;10(suppl_1):S31–S48. [PubMed: 30721958]

128. Han Z, Chen C, Xu X, et al. Dynamic contrast-enhanced CEST MRI using a low molecular weight dextran. NMR Biomed. 2021:e4649. [PubMed: 34779550]

129. de Oliveira JM, van Passel MW, Schaap PJ, de Graaff LH. Proteomic analysis of the secretory response of Aspergillus niger to D-maltose and D-xylose. PLoS One. 2011;6(6):e20865. [PubMed: 21698107]

130. Dubick MA, Wade CE. A review of the efficacy and safety of 7.5% NaCl/6% dextran 70 in experimental animals and in humans. The Journal of trauma. 1994;36(3):323–330. [PubMed: 7511708]

131. Ljungstrom KG. Safety of dextran in relation to other colloids--ten years experience with hapten inhibition. Infusionsther Transfusionsmed. 1993;20(5):206–10. [PubMed: 7508309]

132. Zu Z, Jiang X, Xu J, Gore JC. Spin-lock imaging of 3-o-methyl-D glucose (3o MG) in brain tumors. Med Reson Med. 2018;80(3):1110–1117.

133. Haris M, Cai K, Singh A, Hariharan H, Reddy R. In vivo mapping of brain myo-inositol. Research Support, N.I.H., Extramural. NeuroImage. 2011;54(3):2079–85. [PubMed: 20951217]

134. Cai K, Haris M, Singh A, et al. Magnetic resonance imaging of glutamate. Nat Med. 2012;18(2):302–6. [PubMed: 22270722]

135. Goldenberg JM, Pagel MD, Cardenas-Rodriguez J. Characterization of D-maltose as a T2 -exchange contrast agent for dynamic contrast-enhanced MRI. Magn Reson Med. 2018;80(3):1158–1164. [PubMed: 29369407]

136. Daoust A, Dodd S, Nair G, et al. Transverse relaxation of cerebrospinal fluid depends on glucose concentration. Magn Reson Imaging. 2017;44:72–81. [PubMed: 28782676]

137. Jin T, Kim S-G. Advantages of Chemical Exchange-Sensitive Spin-Lock (CESL) Over Saturation Transfer (CEST) for Hydroxyl- and Amine-Water Proton Exchange Studies. NMR Biomed. 2014;27(11):1313–1324. [PubMed: 25199631]

138. Swift TJ, Connick RE. NMR-relaxation mechanisms of O17 in aqueous solutions of paramagnetic cations and lifetime of water molecules in first coordination sphere. J Chem Phys. 1962;37:307–320.

139. Xu J, Chan KWY, Xu X, Yadav N, Liu G, van Zijl PCM. On-resonance variable delay multipulse scheme for imaging of fast-exchanging protons and semisolid macromolecules. Magn Reson Med. 2017;77(2):730–739. [PubMed: 26900759]

140. Yadav NN, Jones CK, Hua J, Xu J, Van Zijl PC. Imaging of endogenous exchangeable proton signals in the human brain using frequency labeled exchange transfer imaging. Magn Reson Med. 2013;69(4):966–973. [PubMed: 23400954]

141. Friedman JI, McMahon MT, Stivers JT, Van Zijl PC. Indirect detection of labile solute proton spectra via the water signal using frequency-labeled exchange (FLEX) transfer. J Am Chem Soc. 2010;132(6):1813–1815. [PubMed: 20095603]

142. Xu J, Yadav NN, Bar-Shir A, et al. Variable delay multi-pulse train for fast chemical exchange saturation transfer and relayed-nuclear overhauser enhancement MRI. Magn Reson Med. 2014;71(5):1798–812. [PubMed: 23813483]

143. Xu X, Yadav NN, Zeng H, et al. Magnetization transfer contrast–suppressed imaging of amide proton transfer and relayed nuclear overhauser enhancement chemical exchange saturation transfer effects in the human brain at 7T. Magn Reson Med. 2016;75(1):88–96. [PubMed: 26445350]

144. Petersen ET, Mouridsen K, Golay X, all named co-authors of the Qt-rs. The QUASAR reproducibility study, Part II: Results from a multi-center Arterial Spin Labeling test-retest study. NeuroImage. 2010;49(1):104–13. [PubMed: 19660557]

145. Trott O, Palmer Iii AG. Theoretical study of R1ρ rotating-frame and R2 free-precession relaxation in the presence of n-site chemical exchange. J Magn Reson. 2004;170(1):104–112. [PubMed: 15324763]

146. Xu X, Xu J, Chan KWY, et al. GlucoCEST imaging with on-resonance variable delay multiple pulse (onVDMP) MRI. Magn Reson Med. 2019;81(1):47–56. [PubMed: 30058240]

147. Little TJ, McKie S, Jones RB, et al. Mapping glucose-mediated gut-to-brain signalling pathways in humans. NeuroImage. 2014;96:1–11. [PubMed: 24685436]

148. Terpstra M, Gruetter R, High WB, et al. Lactate turnover in rat glioma measured by in vivo nuclear magnetic resonance spectroscopy. Cancer Res. 1998;58(22):5083–8. [PubMed: 9823316]

149. Chen P, Shen Z, Wang Q, et al. Reduced cerebral glucose uptake in an Alzheimers rat model with glucose-weighted chemical exchange saturation transfer imaging. Front Aging Neurosci. 2021;13:618690. [PubMed: 33815088]

150. Xu X, Xu J, Knutsson L, et al. The effect of the mTOR inhibitor rapamycin on glucoCEST signal in a preclinical model of glioblastoma. Magn Reson Med. Jun 2019;81(6):3798–3807. [PubMed: 30793789]

151. Capozza M, Anemone A, Dhakan C, et al. GlucoCEST MRI for the Evaluation Response to Chemotherapeutic and Metabolic Treatments in a Murine Triple-Negative Breast Cancer: A Comparison with[(18)F]F-FDG-PET. Mol Imaging Biol. 2021;24(1):126–134. [PubMed: 34383241]

152. Kentrup D, Bovenkamp P, Busch A, et al. GlucoCEST magnetic resonance imaging in vivo may be diagnostic of acute renal allograft rejection. Kidney Int. 2017;92(3):757–764. [PubMed: 28709641]

153. Wu D, Xu J, Lei J, Mclane M, Van Zijl PC, Burd I. Dynamic glucose enhanced MRI of the placenta in a mouse model of intrauterine inflammation. Placenta. 2018;69:86–91. [PubMed: 30213490]

154. Hartmann B, Müller M, Seyler L, et al. Feasibility of deuterium magnetic resonance spectroscopy of 3-O-methylglucose at 7 Tesla. PLoS ONE. 2021; 16(6):e0252935. [PubMed: 34097707]

155. Gatenby RA, Gillies RJ. Why do cancers have high aerobic glycolysis? Nat Rev Cancer 2004;4(11):891–899. [PubMed: 15516961]

156. Artemov D, Bhujwalla ZM, Pilatus U, Glickson JD. Two-compartment model for determination of glycolytic rates of solid tumors by in vivo 13C NMR spectroscopy. NMR Biomed. 1998;11(8):395–404. [PubMed: 10221582]

157. Mathieu-Daude Y, Vincent M, Valette J, Flament J. Deciphering the compartmental origin of glucoCEST signal using diffusion-weighted CEST-MRS. Proceed of the 31st ISMRM. 2022:0378.

158. Giedde A. Blood-brain glucose transfer. Handb Exp Pharmacol. 1992:65–114.

159. Gruetter R, Novotny EJ, Boulware SD, Rothman DL, Shulman RG. 1H NMR studies of glucose transport in the human brain. J Cereb Blood Flow Metab. 1996;16(3):427–38. [PubMed: 8621747]

160. Du F, Zhang Y, Zhu XH, Chen W. Simultaneous measurement of glucose blood-brain transport constants and metabolic rate in rat brain using in-vivo 1H MRS. J Cereb Blood Flow Metab. Sep 2012;32(9):1778–87. [PubMed: 22714049]

161. Gyngell ML, Michaelis T, Horstermann D, et al. Cerebral glucose is detectable by localized proton NMR spectroscopy in normal rat brain in vivo. Magn Reson Med. 1991;19(2):489–95. [PubMed: 1679190]

162. Rich LJ, Bagga P, Wilson NE, et al. (1)H magnetic resonance spectroscopy of (2)H-to-(1)H exchange quantifies the dynamics of cellular metabolism in vivo. Nat Biomed Eng. 2020;4(3):335–342. [PubMed: 31988460]

163. Xu X, Sehgal AA, Yadav NN, et al. GlucoCEST-based dynamic glucose enhanced (DGE) MRI at 3 T: Early experience in healthy volunteers and brain tumor patients. Magn Reson Med. 2020;84(1):247. [PubMed: 31872916]

164. Cao J, Tang Y, Li Y, Gao K, Shi X, Li Z. Behavioral changes and hippocampus glucose metabolism in APP/PS1 transgenic mice via electro-acupuncture at governor vessel acupoints. Front Aging Neurosci. 2017;9:5. [PubMed: 28174534]

165. Niwa K, Kazama K, Younkin SG, Carlson GA, Iadecola C. Alterations in cerebral blood flow and glucose utilization in mice overexpressing the amyloid precursor protein. Neurobiol Dis. 2002;9(1):61–68. [PubMed: 11848685]
166. Jack CR Jr, Bernstein MA, Fox NC, et al. The Alzheimer's disease neuroimaging initiative (ADNI): MRI methods. J Magn Reson Imaging. 2008;27(4):685–691. [PubMed: 18302232]
167. Luo F, Rustay NR, Ebert U, et al. Characterization of 7-and 19-month-old Tg2576 mice using multimodal in vivo imaging: limitations as a translatable model of Alzheimer's disease. Neurobiol Aging. 2012;33(5):933–944. [PubMed: 20961663]
168. Poisnel G, Herard A-S, El Tayara NET, et al. Increased regional cerebral glucose uptake in an APP/PS1 model of Alzheimer's disease. Neurobiol Aging. 2012;33(9):1995–2005. [PubMed: 22079157]
169. Busche MA, Hyman BT. Synergy between amyloid-beta and tau in Alzheimer's disease. Nat Neurosci. 2020;23(10):1183–1193. [PubMed: 32778792]
170. Iliff JJ, Wang M, Liao Y, et al. A paravascular pathway facilitates CSF flow through the brain parenchyma and the clearance of interstitial solutes, including amyloid β. Sci Trans Med. 2012;4(147):147ra111–147ra111.
171. Peng W, Achariyar TM, Li B, et al. Suppression of glymphatic fluid transport in a mouse model of Alzheimer's disease. Neurobiol Dis. 2016;93:215–225. [PubMed: 27234656]
172. Da Mesquita S, Louveau A, Vaccari A, et al. Functional aspects of meningeal lymphatics in ageing and Alzheimer's disease. Nature. 2018;560(7717):185–191. [PubMed: 30046111]
173. Hessov I, Bojsen-Moller M. Experimental infusion thrombophlebitis. Importance of the pH of glucose solutions. Eur J Intensive Care Med. 1976;2(2):97–101. [PubMed: 9290]
174. World Health Organization. Mean fasting blood glucose. The Global Health Observatory. 2022. https://www.who.int/data/gho/indicator-metadata-registry/imr-details/2380.
175. Kim M, Gillen J, Landman BA, Zhou J, van Zijl PC. Water saturation shift referencing (WASSR) for chemical exchange saturation transfer (CEST) experiments. Magn Reson Med. 2009;61(6):1441–50. [PubMed: 19358232]
176. Schuenke P, Windschuh J, Roeloffs V, Ladd ME, Bachert P, Zaiss M. Simultaneous mapping of water shift and B1 (WASABI)-Application to field-Inhomogeneity correction of CEST MRI data. Magn Reson Med. 2017;77(2):571–580. [PubMed: 26857219]
177. Liebert A, Zaiss M, Gumbrecht R, et al. Multiple interleaved mode saturation (MIMOSA) for B(1) (+) inhomogeneity mitigation in chemical exchange saturation transfer. Magn Reson Med. 2019;82(2):693–705. [PubMed: 31002432]
178. Zaiss M, Herz K, Deshmane A, et al. Possible artifacts in dynamic CEST MRI due to motion and field alterations. J Magn Reson. 2019;298:16–22. [PubMed: 30500568]
179. Simegn GL, Van der Kouwe AJW, Robertson FC, Meintjes EM, Alhamud A. Real-time simultaneous shim and motion measurement and correction in glycoCEST MRI using double volumetric navigators (DvNavs). Magn Reson Med. 2019;81(4):2600–2613. [PubMed: 30506877]
180. Larkman DJ, Hajnal JV, Herlihy AH, Coutts GA, Young IR, Ehnholm G. Use of multicoil arrays for separation of signal from multiple slices simultaneously excited. J Magn Reson Imaging. 2001;13(2):313–7. [PubMed: 11169840]
181. Setsompop K, Feinberg DA, Polimeni JR. Rapid brain MRI acquisition techniques at ultra-high fields. NMR Biomed. 2016;29(9):1198–221. [PubMed: 26835884]
182. Lustig M, Donoho D, Pauly JM. Sparse MRI: The application of compressed sensing for rapid MR imaging. Magn Reson Med. 2007;58(6):1182–95. [PubMed: 17969013]
183. Gamper U, Boesiger P, Kozerke S. Compressed sensing in dynamic MRI. Magn Reson Med. 2008;59(2):365–73. [PubMed: 18228595]
184. Luo H, Zhang T, Gong NJ, et al. Deep learning-based methods may minimize GBCA dosage in brain MRI. Eur Radiol. 2021;31(9):6419–6428. [PubMed: 33735394]
185. Pasumarthi S, Tamir JI, Christensen S, Zaharchuk G, Zhang T, Gong E. A generic deep learning model for reduced gadolinium dose in contrast-enhanced brain MRI. Magn Reson Med. 2021;86(3):1687–1700. [PubMed: 33914965]

186. Miller LP, Villeneuve JB, Braun LD, Oldendorf WH. Effect of pharmacological doses of 3–0-methyl-D-glucose and 2-deoxy-D-glucose on rat brain glucose and lactate. Stroke. 1986;17(5):957–61. [PubMed: 3764967]

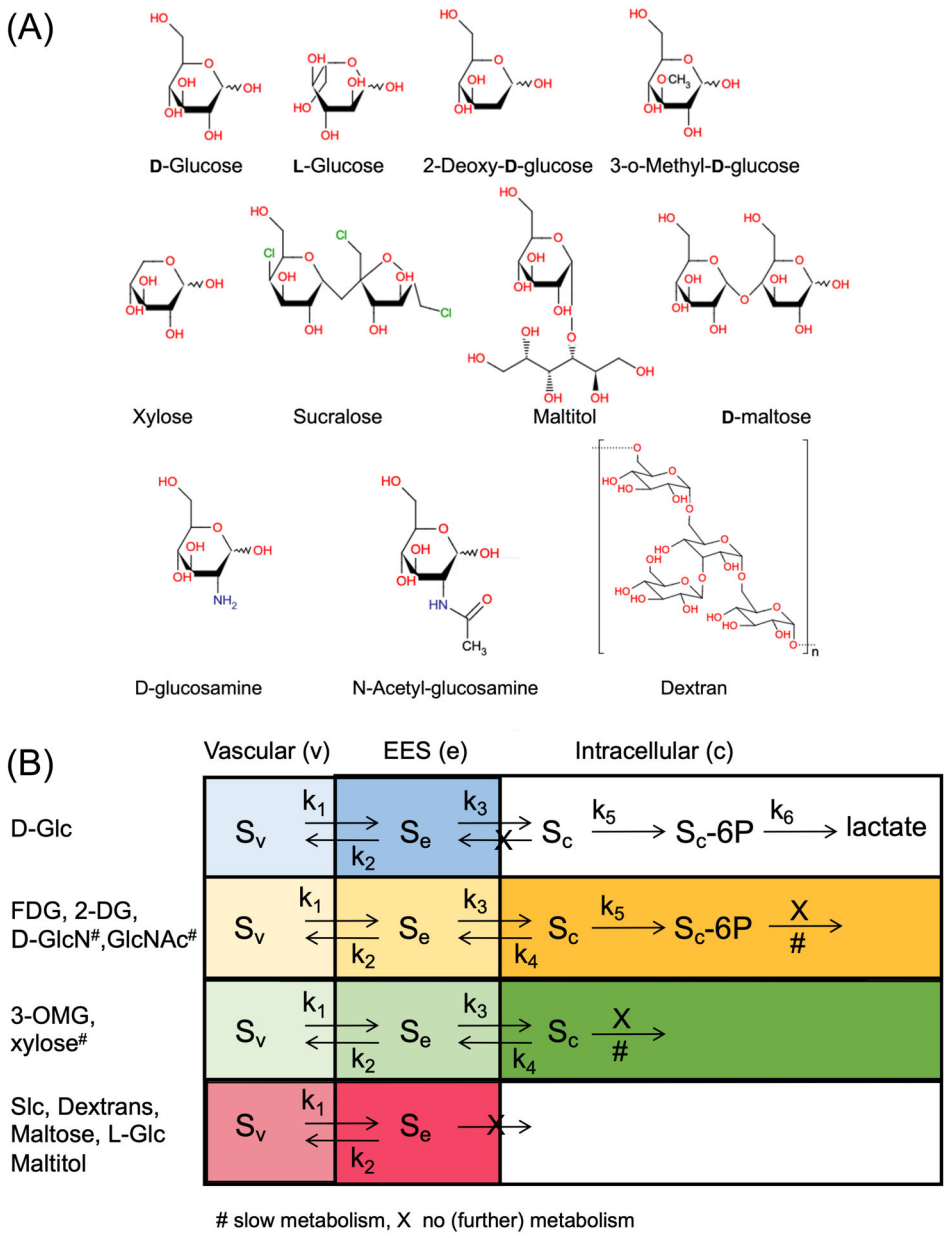

Fig. 1.

(A) Structures of sugars studied as potential contrast agents by exchange-based MRI. **(B)** Overview of compartmental location of sugars (S) and their metabolic products (if any) in tumors, and the rate constants (k) for transport or metabolism. Color indicates relative contrast contribution (Darker color shows increased contribution, white indicates negligible sugar signal). For D-glc, the concentrations in vascular space and EES are comparable, but due to lower pH (See Fig. 2), the EES has a higher signal contribution. Intracellular signal is very small to negligible due to rapid phosphorylation and glycolysis. For 3-OMG and xylose, the signal is predominantly due to trapped intracellular compound, but xylose has very slow metabolism. For FDG, 2-DG, D-GlcN and GlcNAc, the phosphorylated product is the main component measured, but D-GlcN and GlcNAc are metabolized slowly. For

L-Glucose and dimers or larger sugars, the agents occupy only plasma in blood. When they enter the EES, the concentration depends on k_1. For equal concentration, the signal in EES is higher due to the lower pH. Figure 1B *is an extended version of a model presented in Chan et al.*[41] *using physiological information from many references in* Sections 2.1–2.5. *This illustration, which assumes the presence of BBB disruptions, was derived from the model for D-Glc transport and metabolism in normal brain by van Zijl et al*[68]*, which in turn was constructed based on the Sokoloff model for* ^{14}*C-DG uptake for autoradiography.*[67] *Some parts were reproduced with permission from Chan et al. Magn Reson Med 2012;68(6):1764–1773.*[41]

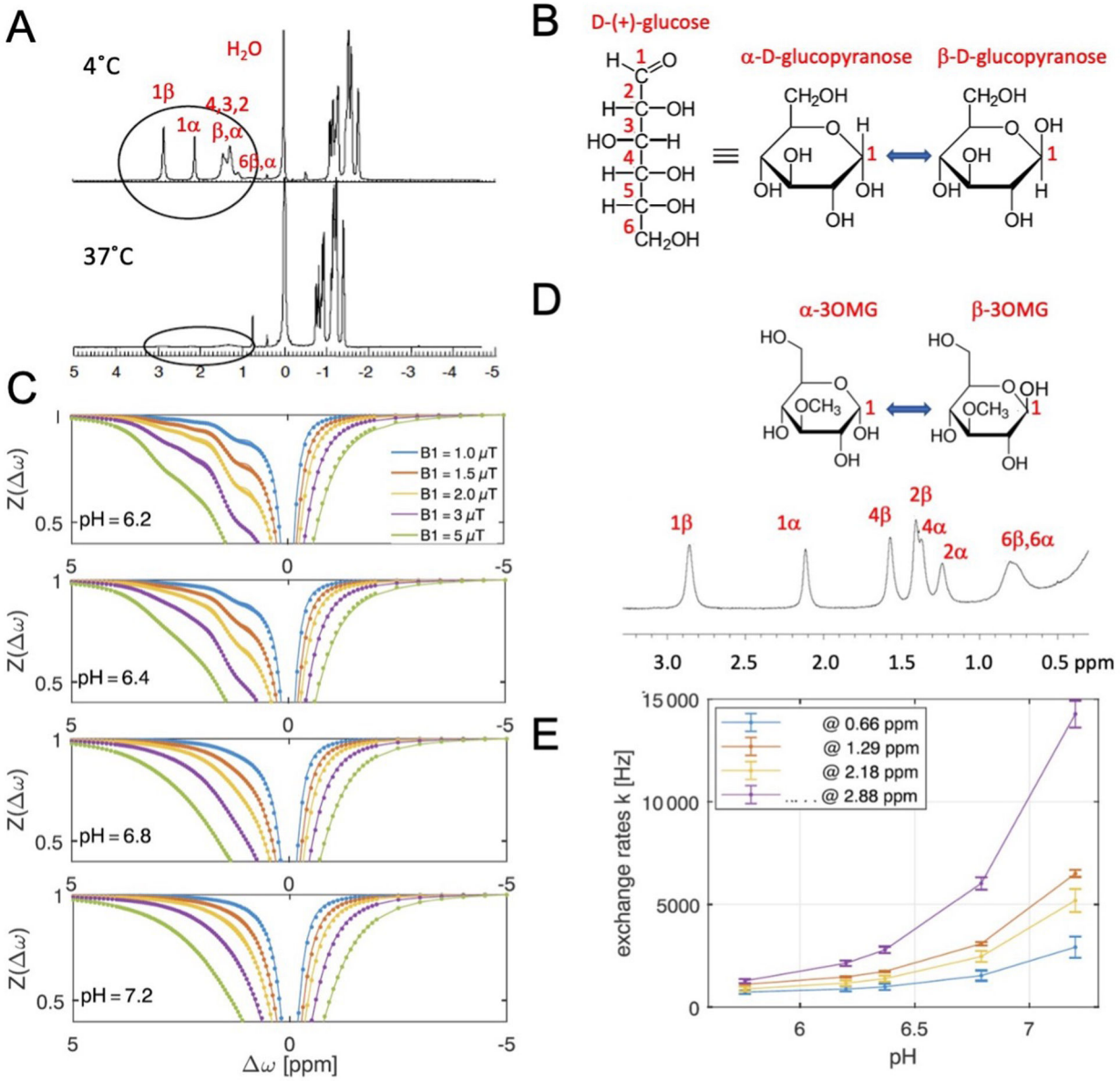

Fig. 2: Structures and spectral features of D-Glc (A-C) and 3-OMG (D) and exchange rates of hydroxyl protons in D-glucose (E).

(A) 11.7T ^{1}H NMR spectrum of D-Glc(300 mM, pH 3.5 in H_2O) at 4 °C and 37 °C. At higher temperature, the visibility of the hydroxyl protons reduces strongly due to the increased exchange rate, while the opposite will occur in Z-spectra. Assignments of the resonances for the two D-Glc anomers **(B)** are also given. **(C)** Z-spectra of 20mM glucose solution in PBS buffer (37°C) acquired at 14.1 T as a function of pH and B_1. At pH = 6.2, some resonances can still be distinguished, but the increased exchange rates at higher pH **(E)** cause a merging of the signals with the water resonance. **(D)** Anomer structures and 11.7T ^{1}H NMR spectrum of 3-OMG (100 mM, pH 5.77 in H_2O) at 4 °C, 24 hours after dissolving α−3-OMG, showing the two anomers with similar resonance frequencies as the D-Glc anomers. **(E)** Estimated exchange rates for four resonance groups in the Z-spectra as a function of pH using a multi-B_1 fits of the data in **(C)**. *Figure parts*

reproduced with permission from Zhou and van Zijl. Prog Nucl Magn Reson Spectrosc 2006;48:109–136[76]*; Zaiss et al, NMR Biomed 2019;32(9):e4113*[51]*; Rivlin et al. Magn Reson Med 2014;72(5):1375–1380.*[57] *Assignment from the first paper was adjusted with recent knowledge from Zaiss et al.*

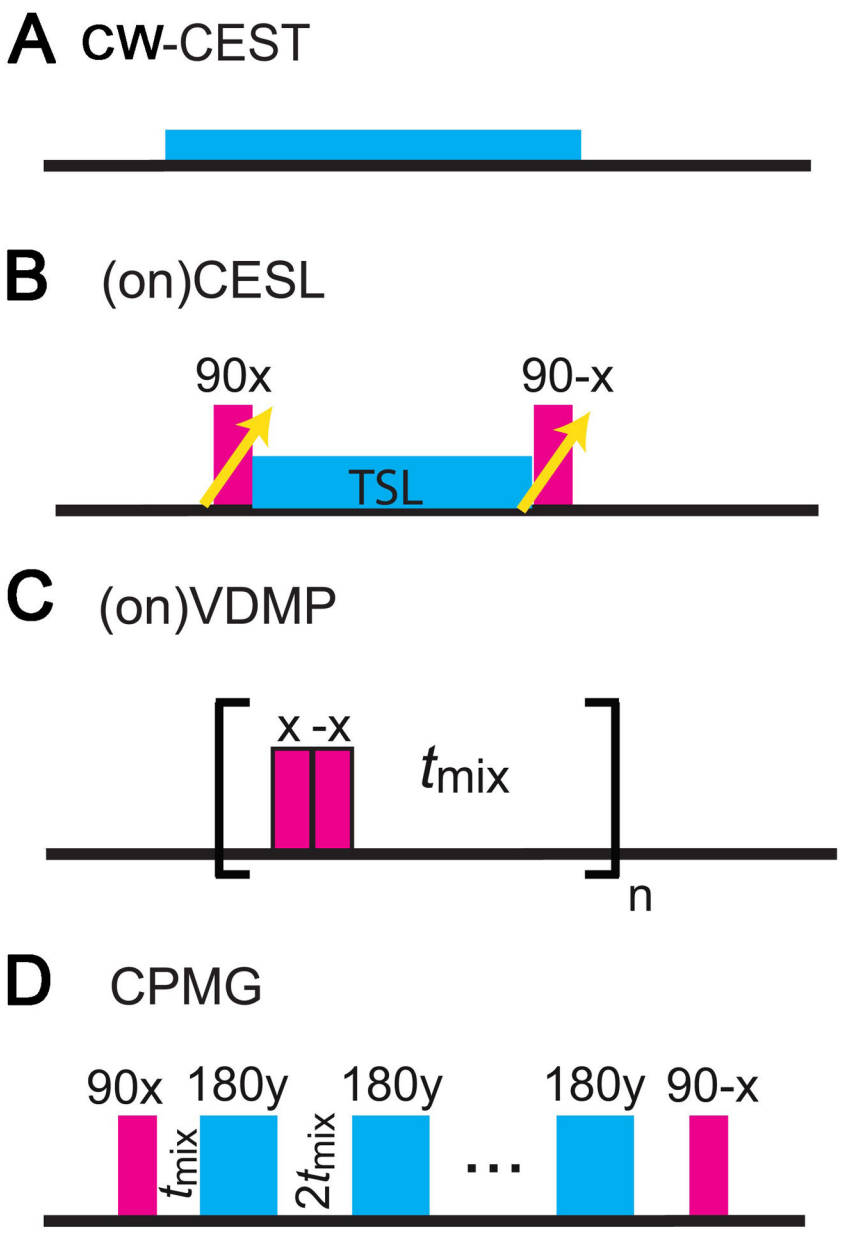

Fig. 3.

Simplified illustration of pulse sequence preparation periods commonly used for DGE MRI. **(A)** continuous wave-CEST: on clinical scanners, usually continuous wave saturation is not possible due to hardware and SAR limits. Instead, a pseudo-continuous wave saturation can be achieved by applying RF irradiation through alternating transmitting channels or using a pulse-train approach in which short delays in between saturation pulses are added. **(B)** on-resonance spin lock, which means the 90 pulses are on resonance to the water frequency. In practice, adiabatic pulses are helpful to avoid B_1 inhomogeneity. **(C)** on-resonance variable delay multi-pulse (onVDMP): the binomial pulse pair is on resonance. The delay, t_{mix}, should be minimized to increase saturation efficiency in DGE MRI. Phase cycling of binomial pulses can be used to reduce image artifacts caused by B_1 inhomogeneity. **(D)**

Carr-Purcell-Meiboom-Gill (CPMG) sequence: t_{mix} values of 6 ms and 111 ms have been used to measure the DGE signal in the brain parenchyma and CSF at 3T, respectively,[19] while a t_{mix} of 10ms was used to assess T_2 effects with DGE.[17]

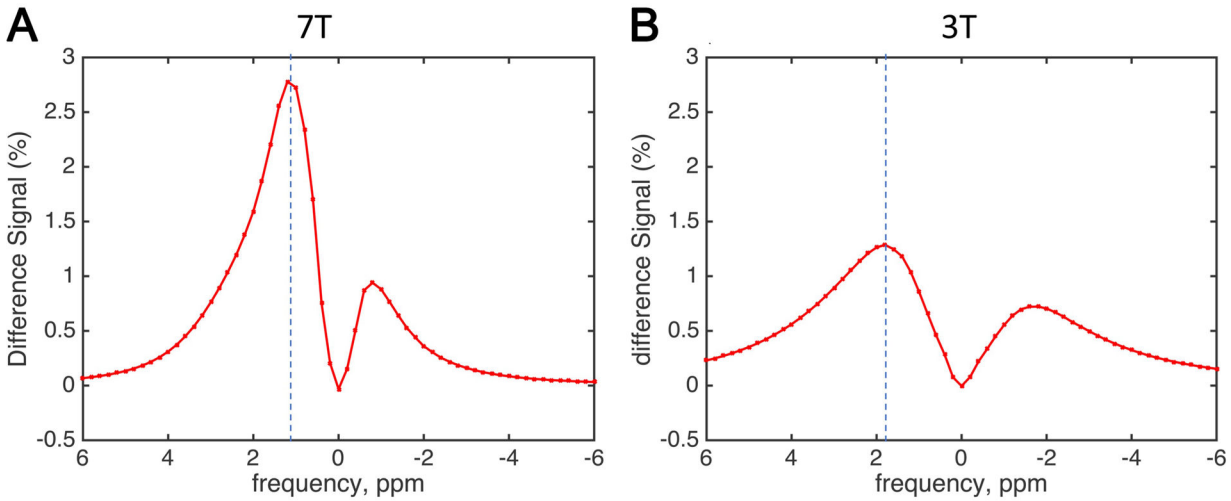

Fig. 4. Simulation of the effect of peak coalescence between hydroxyl and water protons on the DGE signal difference at different fields.

The concentration of D-Glc was assumed to be increased by 10 mM, and the water T_2 reduced by 1% due to the glucose infusion. The difference spectra were calculated by taking the difference between the pre-infusion and the post-infusion Z-spectra at **(A)** 7T and **(B)** 3T. *For a more comprehensive simulation, taking into account of the effect of B_1 and different tissue types, please refer to* Fig 1 *of Xu et al. Magn Reson Med. 2020;84(1):247–262.*[53]

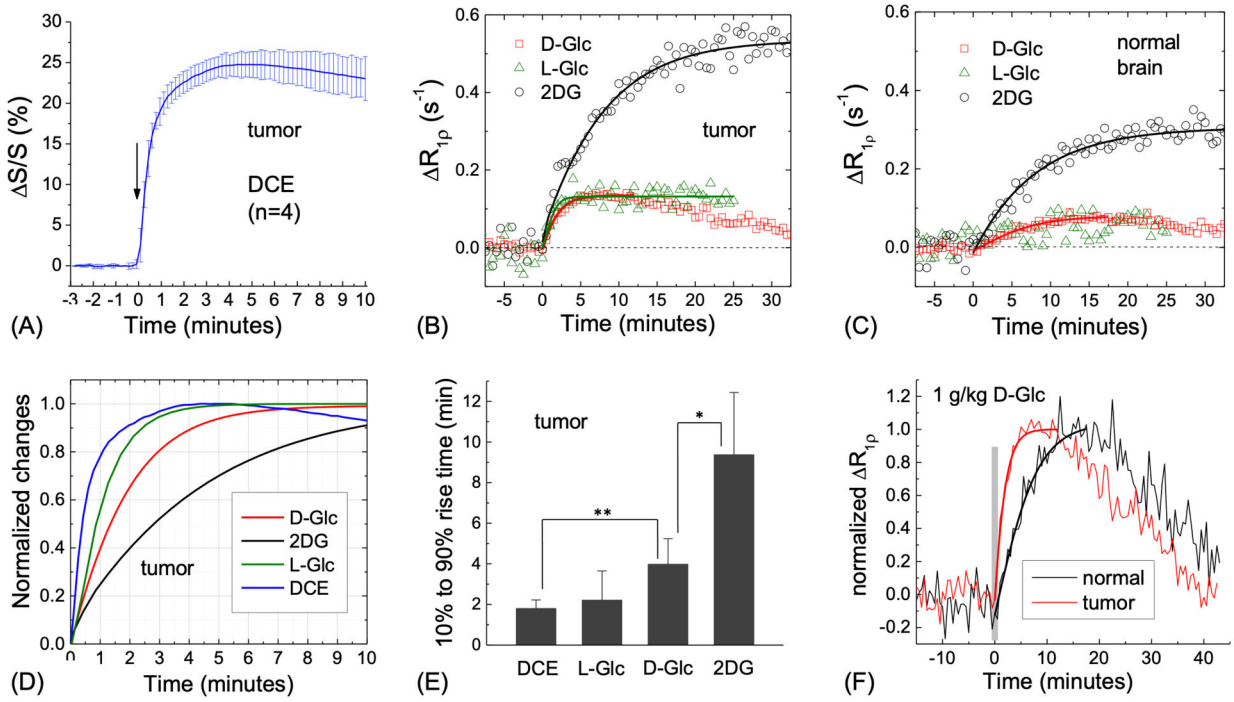

Fig. 5.

Comparison of time courses (DCE and $\Delta R_{1\rho}$ based DGE) for contrast agent uptake in a 9L-glioma rat model. **(A)** DCE after GdDTPA injection (n = 4). **(B,C)** DGE time courses for 0.25 g/kg of 2-DG, 0.25 g/kg of L-Glc, and 1 g/kg of D-Glc (scaled down by a factor of 4 to correspond to 0.25 g/kg D-Glc) to allow visual comparison. The initial parts of the curves were fitted to Sigmoid functions. (B) ROI in the tumor, showing equal fast early delivery for all sugars. L-Glc should reflect signal in extracellular space (Vessels + EES, See Fig. 1B). D-Glc and L-Glc delivery lead to similar maximum signal, indicating D-Glc similar compartmental origin. However, D-Gl reaches maximum signal slower, which we attribute to transport into the cell and fast metabolism to lactate (not detected). This is supported by D-Glc signal reducing further when substrate runs out. 2-DG signal reflects extracellular and intracellular space, continuously increasing due to build-up of the phosphorylated product. (C) ROI in contralateral brain, assumed to be normal. Both 2-DG and D-Glc signal are about halved compared to tumor, while L-Glc signal is small (noisy), but not negligible. In this case, L-Glc should be due mainly to blood vessels and D-Glc to vessels + EES, but normal brain EES has reduced D-Glc (factor of about 4 due to facilitated transport). **(D-F)** normalized time course comparisons. **(D)** DCE has the fastest time to peak, while 2-DG has the slowest. **(E)** Comparison of the 10 to 90% rise time for DGE MRI and CESL with L-Glc, D-Glc, and 2-DG injections. *: $p<0.05$, **: $p<0.01$. (F) The D-Glc time course in tumor is faster than normal brain, attributed to BBB breakdown. *Reproduced, with permission from Jin et al. Magn Reson Med. 2018;80(2):488–495*[49]; Parts (B), (C), and (F) were kindly generated upon our request by Dr. Tao using the original data.

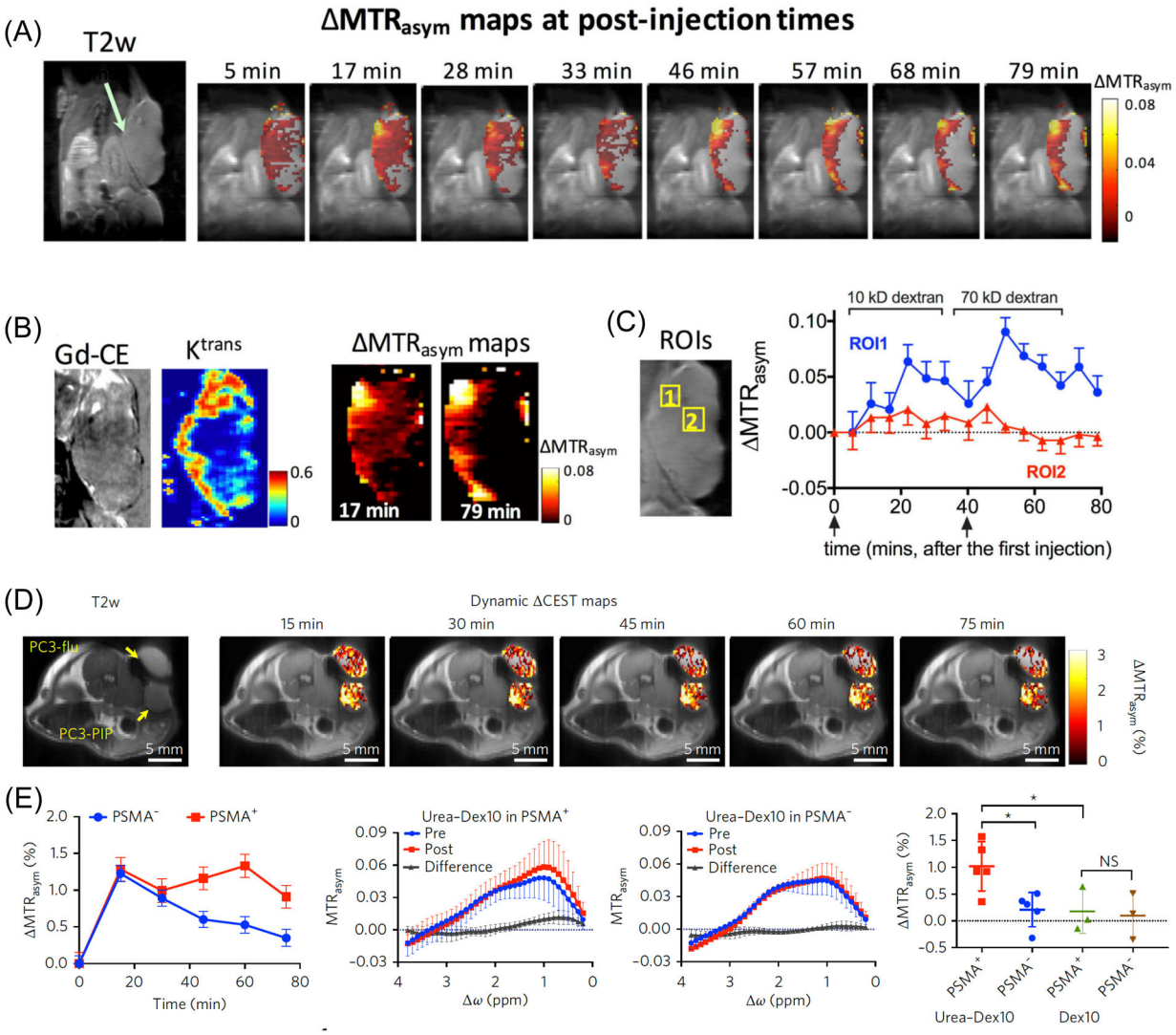

Fig. 6. Characterization of vessel permeability using multiple dextran sizes (A-C) and PSMA targeted dextran CEST MRI (D,E).

(A) Anatomical T2w images and dynamic dexCEST MRI showing distinctive tumor uptake of 10 kD and 70 kD dextran (administered at t = 0 and t = 40 min, resp) in terms of spatial distribution and pharmacokinetics. **(B)** Zoomed view of a Gd contrast-enhanced image, permeability-sensitive (K^{trans}) map, and corresponding ΔMTR_{asym} maps at 17 and 79 minutes, respectively, in the same rat. **(C)** Dynamic change of the dexCEST signal in the two ROIs (marked in zoomed view of T2w image on the left). **(D) Urea conjugated dextran for PSMA targeting** Changes in the dynamic CEST signal in PSMA+ and PSMA– tumors. T2-weighted (T2w) image (left) and dynamic CEST maps (right) at 1 ppm after the injection of 375 mg per kg urea–Dex10 (injection volume = 100 μl). **(E)** Mean changes in the CEST signal in PSMA+ and PSMA– tumors in one of the mice for which time dependence was measured (left). The error bars are the standard errors of the CEST signal of all the pixels in each tumor. All CEST images were acquired using a 1.8 μ T and continuous-wave pulses that were 3 s long. Average CEST signal in the tumor for five mice before and 1 h after the injection of urea–Dex10 (middle). Error bars are standard deviations of the CEST signal

of all five tumors. Column scatter plots (right) show the mean changes in CEST signal as quantified by ΔMTR_{asym} (1 h) in each tumor type (n = 5 and n = 3 for urea–Dex10 and non-targeted Dex10, respectively). *P < 0.05 (Student's t-test two-tailed and unpaired) *Figure parts reproduced with permission from Li et al. Magn Reson Med 2018;79(2):1001–1009.*[32]*; Liu et al. Nat Biomed Eng 2017;12(1);977–982.*[31];

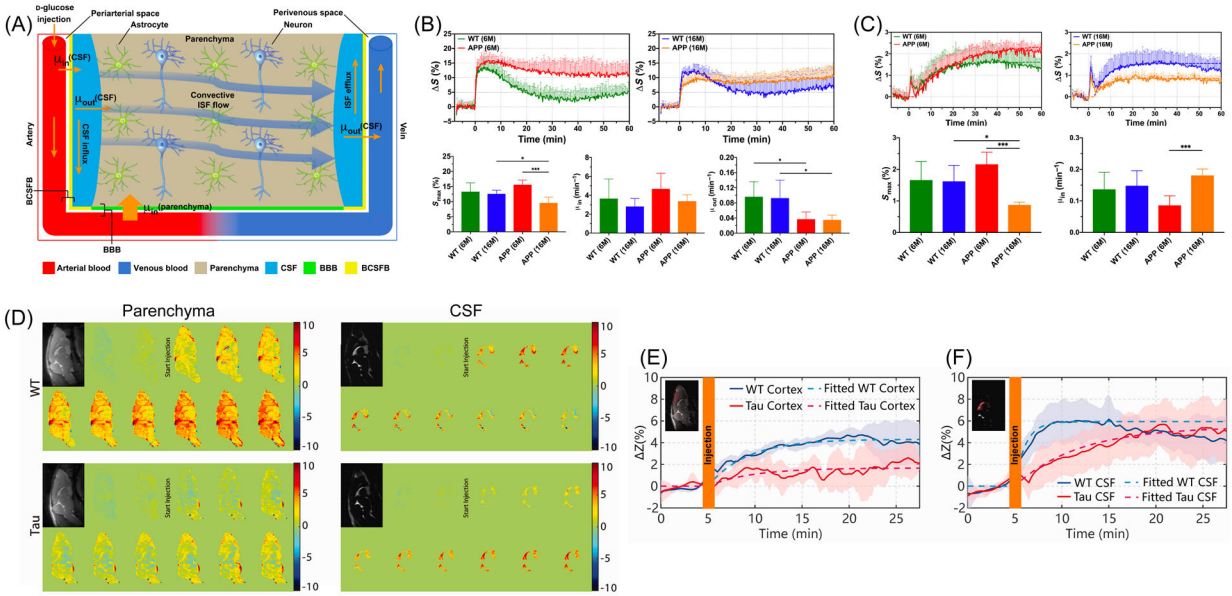

Fig. 7. DGE MRI of Alzheimer's disease.

(A) Schematic diagram of the glucose transportation in the brain. Glucose from the artery enters parenchyma brain and CSF through glucose transporters in the periarterial space, including glucose transporters in blood-CSF barrier (BCSFB) and BBB. A large portion of CSF recirculates to the parenchyma brain and finally drains interstitial fluid (ISF) clearance. μ_{in}, uptake rate; μ_{out}, clearance rate. **(B)** Experimental (solid line) and fitted (dashed line) parenchymal DGE curves for WT (6 months, n = 5; 16 months, n = 5) and APP/PS1 (6 months, n = 5; 16 months, n = 5) mice. **(C)** Experimental (solid line) and fitted (dashed line) CSF DGE curves for WT (6 months, n = 5; 16 months, n = 5) and APP/PS1 (6 months, n = 5; 16 months, n = 5) mice. **(D)** Dynamic AUC maps for WT and Tau mice over the 27.5 min DGE experiment, in both parenchyma and CSF. The brain tissue maps were recorded using the onVDMP sequence with 12 binomial pulse pairs (parenchyma), while the CSF maps were obtained with 100 binomial pulse pairs (CSF). Each dynamic AUC map was calculated by averaging 10 successive DGE images, which lead to a time window of 150 s. The averaged time-resolved DGE curves for the **(E)** cortex and **(F)** CSF of WT and Tau mice. *Figure parts reproduced with permission from Huang et al. Sci Adv 2020;6(20):eaba3884*[79] *and Chen et al. J Cereb Blood Flow Metab 2021;41(5):1013–1025.*[80]

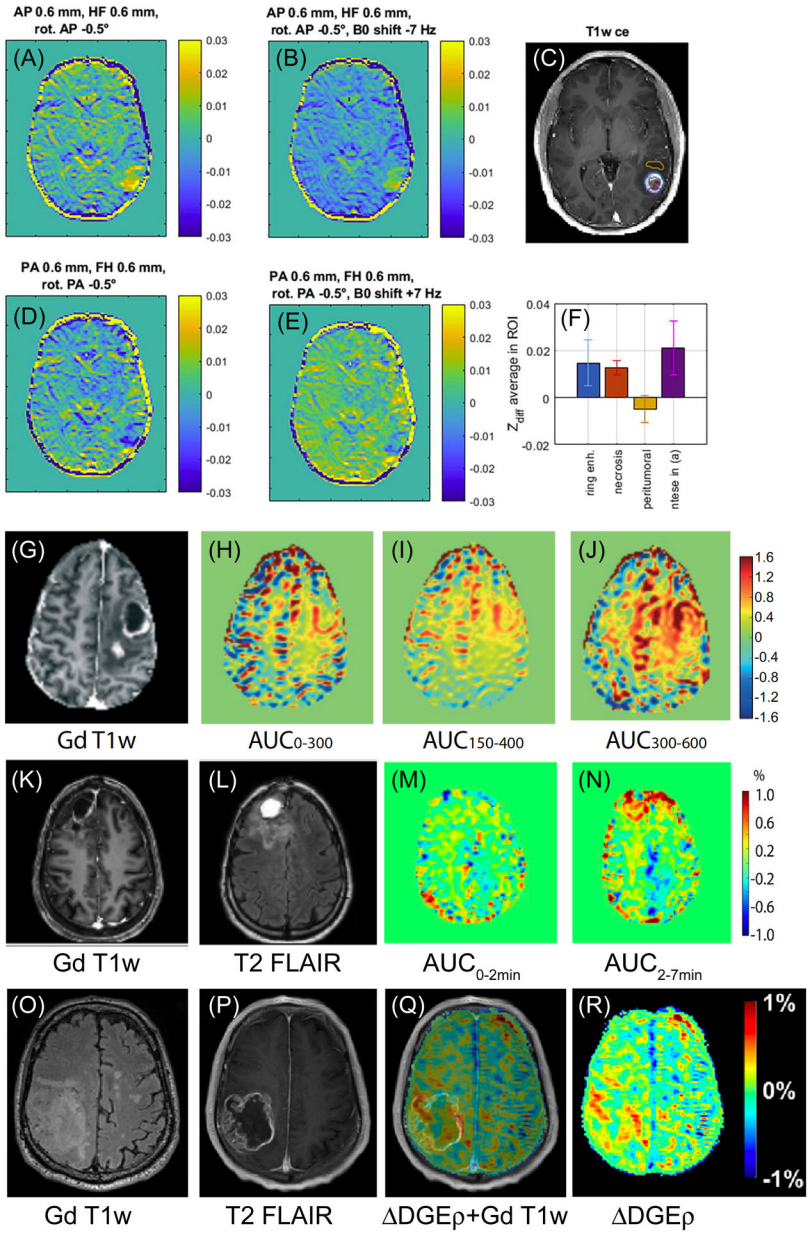

Fig. 8. Examples of human DGE studies.

(A-F) DGE images of a brain tumor patient without glucose injection at 3T show the effect of motion creating so called “pseudo-CEST effects”. The difference maps between pre-motion and post-motion were generated to simulate DGE contrast **(A,D)** together with B_0 shifts **(B,E)**. Both hyper- and hypointensities are seen in the tumor region in the DGE images, similar to the Gd contrast-enhancement **(C)**. This demonstrate that motion artifacts in DGE in tumor areas can be mistaken as uptake signal. **(F)** ROI analysis revealed pseudo CEST effect in tumor sub-regions. **DGE imaging in a brain tumor patient at 7T.** Gd-T1w image **(G)** and DGE based AUC images **(H-J)** for different time periods relative to the start of infusion at 7T. The DGE shows a faster uptake in the rim around the necrotic region and with a slower uptake in the tumor center and surrounding tissue. **(K - R) DGE**

imaging in brain tumor patient at 3T. First row: Gd-T1w images **(K)** and DGE based AUC images **(M,N)** for different time periods relative to the start of infusion. The increased DGE signal corresponds with the enhanced Gd location, particularly toward the later phase of the DGE imaging. Second row: T2 FLAIR **(O)**, Gd-T1w **(P)**, Gd-T1w with overlaid ΔDGEρ map **(Q)** and the ΔDGEρ map **(R)**. These early images support potential for DGE MRI if higher SNR can be achieved. *Figure parts reproduced with permission from Zaiss M, et al. J Magn Reson. Jan 2019;298:16–22;*[189] *Xu et al. Tomography. 2015;1(2):105–114;*[45]; *Xu et al. Magn Reson Med. 2020;84(1):247–262.*[53]; *Herz et al. Magn Reson Med. 2019; 82(5):1832–1847*[52]

Table 1.

Exchange-based studies using D-glucose (D-Glc), deoxyglucose (2-DG) and 3-o-methyl-D-glucose (3-OMG) as contrast agent.

Organ	Condition	Species	B_0 (T)	Method, offset frequency	Dose (g/kg)	Study
D-glucose						
Brain	**Healthy**	C57BL/6 mouse	3	glucoCEST CPMG/ onVDMP/onCESL DGE (on-resonance)	2.5, 1.25, 0.63	Huang J, et al. 2021[19]
		Rat	9.4	CESL, DGE (on-resonance)	0.075, 0.5, 1.0	Jin T, et al. 2014[43]
		Human	7	glucoCEST DGE (1.2 ppm)	~0.38	Knutsson L, et al. 2018[48]
			3	glucoCEST DGE (1.0 ppm, 2.0 ppm)	~0.38	Seidemo A, et al. 2021[54]
	AD APP/PS1	C57BL/6	11.7	glucoCEST onVDMP, DGE (on-resonance)	3.125	Chen L, et al. 2021[80]
	Tau	mouse	3	glucoCEST onVDMP, DGE (on-resonance)	~2.5	Huang J, et al. 2020[79]
	Aβ protein	Rat	7	glucoCEST, 0.9 ppm	~0.0012	Chen P, et al. 2021[149]
	Cancer U87EGFRvIII	SCID mouse	11.7	glucoCEST DGE (1.2 ppm)	~2.5	Xu X, et al. 2015[44]
	U87EGFRvIII		11.7	glucoCEST DGE, (1.2 ppm)	~2.5	Xu X et al. 2019[150]
	9L glioma		11.7	glucoCEST, onVDMP, DGE (1.2 ppm) DGE (on-resonance)	~2.5	Xu X et al. 2019[146]
	glioma	Human	7	glucoCEST DGE (1.2 ppm)	~0.38	Xu X, el al. 2015[45]
	glioblastoma			CESL DGE, (on-resonance)	0.26	Paech D, et al. 2017[46]
	glioblastoma			CESL DGE (on-resonance)	~0.31	Schuenke P, et al. 2017[47]
	gliosarcoma			CESL DGE (on-resonance)	~0.31	Schuenke P, et al. 2017[64]
	glioblastoma			CESL DGE (on-resonance)	~0.31	Boyd PS, et al. 2020[66]
	glioblastoma		3	CESL DGE (0.6,0.9, 1.2,1.5 ppm)	0.3	Herz K, et al. 2019[52]
	glioma			glucoCEST DGE (2.0,1.5 ppm)	~0.38	Xu X, et al. 2020[53]
Breast	**Cancer** MDA-MB-231/ MCF-7	Nude mouse	11.7	glucoCEST, CW-CEST (0.8–2.2 ppm)	2.5	Chan KWY, et al. 2012[41]
	-TS/A	BALB/c mouse	9.4, 7, 3	CESL (1.2 ppm)	3	Zaiss M, et al. 2019[51]
	-4T1	BALB/c mouse	7	glucoCEST, CW-CEST (1.2 ppm)	3	Capozza M, et al. 2021[151]

Colon	**Cancer** -LS174T -SW1222	Nude mouse	9.4	glucoCEST, (0.5–4 ppm)	~0.17	Walker-Samuel S, et al. 2013[42]
Head/Neck	**Cancer**	Human	3	glucoCEST, (1.12–5.03 ppm)	20 mL, unknown	Wang J, et al. 2016[63]
Kidney	**Renal transplant**	Rat	9.4	glucoCEST, (1.0–2.4 ppm)	2.68	Kentrup D, et al. 2017[152]
Lymph/ Prostate	**Cancer**	Human	3	glucoCEST DGE, (2–3 ppm)	0.34	Kim M, et al. 2019[50]
Placenta	**Healthy**	CD-1 mouse	11.7	glucoCEST onVDMP, DGE (on-resonance)	2.5	Wu D, et al. 2018[153]
		Human	3	glucoCEST, (0.75–4 ppm)	0.77	Luo J, et al. 2019[65]
2-Deoxy-D-glucose						
Brain	**Healthy**	Rat	9.4	glucoCEST, DGE (1.0 ppm)	1.0, 0.5	Nasrallah FA, et al. 2013[55]
				CESL, DGE (on-resonance)	1, 0.5, 0.25	Jin T, et al. 2016[56]
	AD	Mouse	7	glucoCEST, DGE (1.2 ppm)	0.5	Tolomeo D et al. 2018[83]
	Cancer 9L glioma	Rat	9.4	CESL, DGE (on-resonance)	1, 0.5, 0.25	Jin T, et al. 2018[49]
			7	CESL, on-resonance	1	Zu Z, et al, 2014[81]
Breast	**Cancer** DA3	BALB/C mouse	7	glucoCEST DGE (1.2 ppm)	2	Rivlin M, et al. 2013[82]
3-o-methyl-D-Glucose						
Brain	**Cancer** U87 glioma	SCID mouse	11.7	glucoCEST, (1.2 ppm)	3	Sehgal AA et al. 2018[59]
	glioblastoma	Rat	9.4	CESL (on-resonance)	1.5	Zu Z et al. 2018[132]
	Stroke	Wistar rat	9.4	CESL, (on-resonance)	1, 4	Jin T, et al. 2018[58]
Breast	**Cancer** DA3-D1-DMBA-3	BALB/C Mouse	7	glucoCEST, (1.2 ppm)	1.5	Rivlin M, et al. 2014[57]
	D1-DMBA-3	BALB/C mouse	7	glucoCEST, (1.2 ppm)	0.45, 0.57, 0.7, 0.75, 1, 1.5, 3.0	Rivlin M, et al. 2018[102]
	MDA-MB-231	RNU rat	7	Deuteration MRS, 3.5 ppm	0.89	Hartmann B et al. 2021[154]
Skin	**Cancer** B16-F10	C57BL/6 mouse	7	glucoCEST, (1.2 ppm)	1.5, 3	Anemone A et al. 2021[60]
NA	**In vitro** 3-OMG solution	NA	11.7	glucoCEST, 1.2, 2.1, 2.8 ppm	NA (20 mM)	Rivlin M, et al. 2018[103]

NA Not applicable.